

# Considerations and recent advances in nanoscale interfaces with neuronal and cardiac networks

Cite as: Appl. Phys. Rev. **8**, 041317 (2021); <https://doi.org/10.1063/5.0052666>

Submitted: 01 April 2021 • Accepted: 07 October 2021 • Published Online: 15 November 2021

 Youngbin Tchoe,  Jihwan Lee,  Ren Liu, et al.

## COLLECTIONS

 This paper was selected as Featured



View Online



Export Citation



CrossMark



Applied Physics  
Reviews

Read. Cite. Publish. Repeat.

**19.162**

2020 IMPACT FACTOR\*

# Considerations and recent advances in nanoscale interfaces with neuronal and cardiac networks

Cite as: Appl. Phys. Rev. **8**, 041317 (2021); doi: [10.1063/5.0052666](https://doi.org/10.1063/5.0052666)

Submitted: 1 April 2021 · Accepted: 7 October 2021 ·

Published Online: 15 November 2021



Youngbin Tchoe,<sup>1</sup>  Jihwan Lee,<sup>1</sup>  Ren Liu,<sup>1</sup>  Andrew M. Bourhis,<sup>1</sup>  Ritwik Vatsyayan,<sup>1</sup>   
Karen J. Tonsfeldt,<sup>1,2</sup>  and Shadi A. Dayeh<sup>1,3,4,a)</sup> 

## AFFILIATIONS

<sup>1</sup>Integrated Electronics and Biointerfaces Laboratory, Department of Electrical and Computer Engineering, University of California San Diego, La Jolla, California 92093, USA

<sup>2</sup>Department of Obstetrics, Gynecology, and Reproductive Sciences, Center for Reproductive Science and Medicine, University of California San Diego, La Jolla, California 92093, USA

<sup>3</sup>Department of Neurological Surgery, University of California San Diego, La Jolla, California 92093, USA

<sup>4</sup>Graduate Program of Materials Science and Engineering, University of California San Diego, La Jolla, California 92093, USA

<sup>a)</sup> Author to whom correspondence should be addressed: [sdayeh@eng.ucsd.edu](mailto:sdayeh@eng.ucsd.edu)

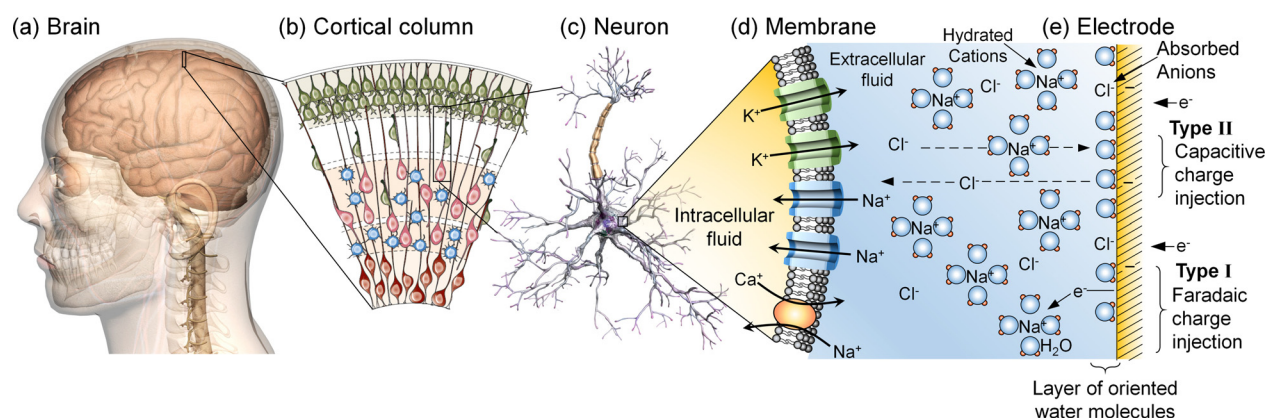
## ABSTRACT

Nanoscale interfaces with biological tissue, principally made with nanowires (NWs), are envisioned as minimally destructive to the tissue and as scalable tools to directly transduce the electrochemical activity of a neuron at its finest resolution. This review lays the foundations for understanding the material and device considerations required to interrogate neuronal activity at the nanoscale. We first discuss the electrochemical nanoelectrode-neuron interfaces and then present new results concerning the electrochemical impedance and charge injection capacities of millimeter, micrometer, and nanometer scale wires with Pt, PEDOT:PSS, Si, Ti, ITO, IrO<sub>2</sub>, Ag, and AgCl materials. Using established circuit models for NW-neuron interfaces, we discuss the impact of having multiple NWs interfacing with a single neuron on the amplitude and temporal characteristics of the recorded potentials. We review state of the art advances in nanoelectrode-neuron interfaces, the standard control experiments to investigate their electrophysiological behavior, and present recent high fidelity recordings of intracellular potentials obtained with ultrasharp NWs developed in our laboratory that naturally permeate neuronal cell bodies. Recordings from arrays and individually addressable electrically shorted NWs are presented, and the long-term stability of intracellular recording is discussed and put in the context of established techniques. Finally, a perspective on future research directions and applications is presented.

Published under an exclusive license by AIP Publishing. <https://doi.org/10.1063/5.0052666>

## TABLE OF CONTENTS

I. INTRODUCTION .....	1	A. Effect of Nanowire geometry for intracellular capabilities .....	16
II. INTRODUCTION TO ELECTROPHYSIOLOGICAL INTERROGATION OF NEURONS.....	2	B. Cell culture viability modulation via substrate material and preparation .....	16
III. ELECTROCHEMICAL CHARACTERISTICS OF ELECTRODES ACROSS MATERIALS AND LENGTH SCALES.....	4	VIII. EXPERIMENTAL VALIDATION OF THE CRITICAL IMPORTANCE OF SINGLE VS MULTIPLE NANOWIRES PER ELECTRODE.....	17
IV. THE NANOWIRE-NEURON JUNCTION.....	6	IX. VALIDATING THE ELECTROPHYSIOLOGICAL ORIGIN OF POTENTIALS RECORDED BY NANOWIRE INTERFACES.....	17
V. RECENT PROGRESS IN NANOWIRE-NEURON ELECTROPHYSIOLOGICAL RECORDINGS.....	8	X. CONCLUSION AND OUTLOOK .....	20
VI. FABRICATION METHODS FOR INTRACELLULAR NANOWIRES.....	11		
VII. NANOELECTRODE-CELL INTERFACE FORMATION METHODS AND RECORDING STABILITY .....	14	I. INTRODUCTION	
		The human brain is composed of nearly a hundred billion neurons and a quadrillion synapses that coordinate our consciousness and	



**FIG. 1.** The human brain and its constituents at multiple length scales interact electrochemically with interrogating electrophysiological probes. Schematic illustrations of (a) human brain, (b) cortical column, (c) neuron, (d) neuronal membrane with channel proteins and lipid bilayers, and (e) interrogating electrode surface. Edited and reprinted with permission from Florio *et al.*, *Curr. Opin. Neurobiol.* **42**, 33 (2017). Copyright 2017 Elsevier. Edited and reprinted with permission from D. R. Merrill, *Implantable Neural Prostheses* (Springer, 2010), Vol. 2, pp. 85–138. Copyright 2010 Springer.<sup>24</sup>

behavior.<sup>1–3</sup> As can be observed in Fig. 1, this activity is fundamentally electrochemical in nature, thus tools to directly investigate said activity must be capable of transducing the resulting electrical potentials with fine spatial and temporal resolution. Short- and long-range perturbations of the electrochemical environment of the brain modulate neuronal network activity to produce function.<sup>4</sup> Furthermore, these neuronal networks are organized in columnar structures composed of layers that are interwoven to be capable of synchronized function.<sup>5–7</sup> Ion channels distributed across the membrane of individual neurons give rise to local ionic currents that determine the resting membrane potential of a cell. This potential can oscillate depending on subthreshold currents and dictates whether an incoming stimulus results in an action potential, and consequently how far electrophysiological events travel across networks. While the all-or-none action potential is considered the currency of the nervous system, it is the result of these subthreshold potentials that are not easily measured at a spatial resolution greater than a few cells. Clearly, an in-depth understanding of coordinated neuronal activity at a finer resolution than the action potential depends on our ability to measure subthreshold oscillations from a large number of neurons and across networks. These oscillations also underscore healthy or impaired function and their interrogation will allow us to both understand neurodegenerative and neuropsychiatric diseases that are associated with ion channel dysfunction<sup>8–12</sup> and to develop drugs and therapies to combat these diseases.

## II. INTRODUCTION TO ELECTROPHYSIOLOGICAL INTERROGATION OF NEURONS

While there are multiple modalities to investigate the nervous system,<sup>13–16</sup> electrophysiology is the gold standard to obtain a detailed understanding of broadband neuronal activity. Neural activity is electrochemical in nature; it originates from ion movement through ion channels on the neuron. Among the diverse set of technologies developed to measure neuronal activity,<sup>16–19</sup> the direct measurement is accomplished by an electrochemically sensitive interface [Figs. 1(d) and 1(e)].<sup>20,21</sup> Ionic current flow both within a single neuron and through a network through electrochemical gradients and field-driven charged-ion movements both directly correlate with current flow established by electron and hole charge transport in the interrogating probe,<sup>22,23</sup> providing high

spatiotemporal resolution. Electrical interrogation can capture the minuscule signals of a single neuron with superior spatial and temporal resolution that well exceeds the capabilities of other methods.

The interface at which this electrochemical activity is sensed is governed by two types of charge-transduction mechanisms, Faradaic (type I), as illustrated in Fig. 1(e).<sup>24,25</sup> Type I is a direct charge transfer through a redox reaction that is typically reversible under recording modalities and is desired to be reversible under stimulation modalities. The presence of dipoles within the surface of the electrode (e.g., at sharp corners and edges) can help facilitate ionization and charge transfer through this Faradaic mechanism. Type II is capacitive in nature and relies on charge screening through the accumulation of a sheet of charged ions on the electrode surface and a sheet of oppositely charged electrons or holes at the electrode surface. Large surface area, conventionally obtained through roughened surfaces, plays a critical role in increasing the capacitance of this interface, thus increasing sensitivity. The purpose of this review is to overview progress and provide the scientific foundations for recording neuronal activity with nano-scale probes, hereafter referred to as nanoelectrodes.

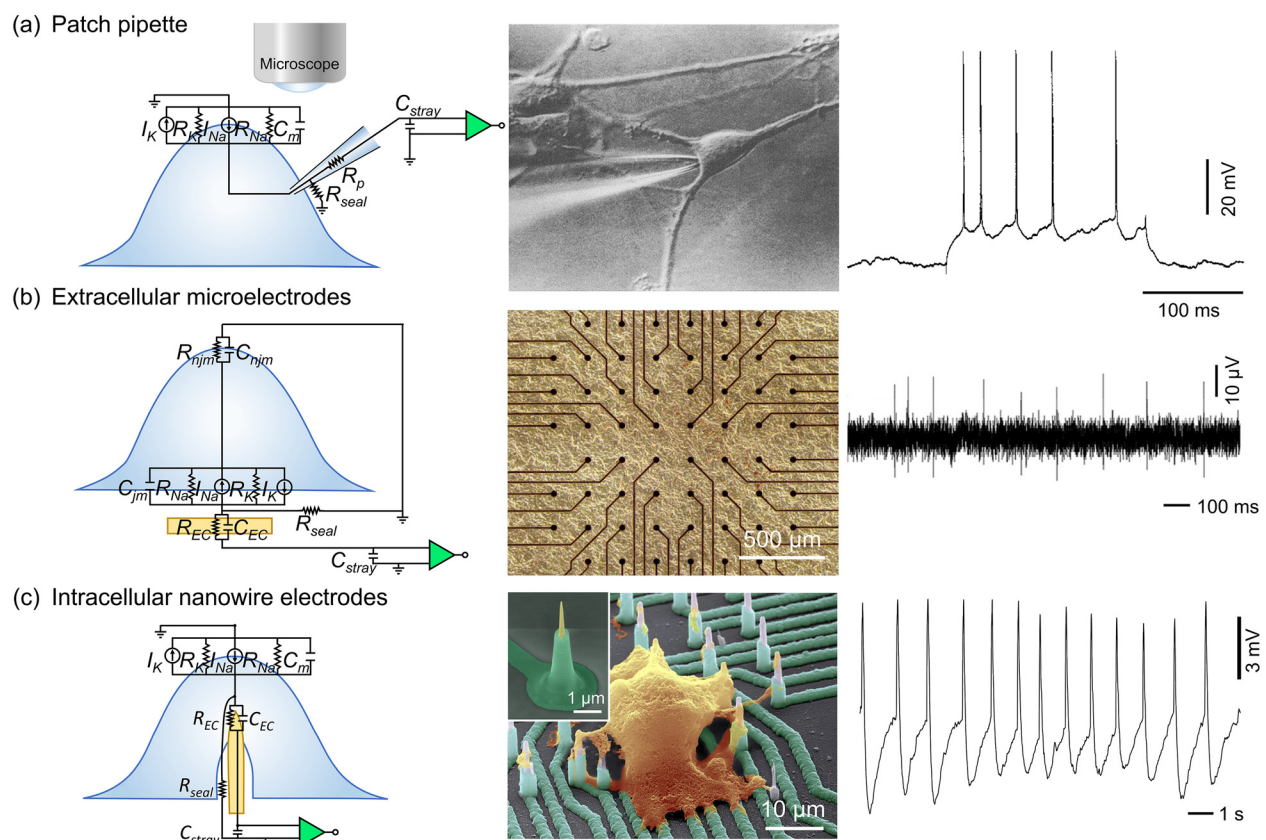
To record intracellular and subthreshold potentials, the gold standard method is the whole-cell patch clamp technique<sup>25</sup> that utilizes a glass micropipette to access the intracellular medium. Patch clamp's intracellular access enhances the signal coupling efficiency and captures the broadband neuronal activity with high temporal resolution.<sup>26</sup> Patch clamp electrode forms a leak-tight giga-ohm seal between the cellular membrane and the micropipette orifice. This high resistance seal allows low background thermal noise and reliable voltage clamping, i.e., fixing membrane potential at a desired level<sup>27</sup> to provide high-fidelity recording. Neher *et al.* pioneered single ion channel recording using patch clamp<sup>28,29</sup> and paved the way to study and regulate ion channel behaviors and mechanisms, including modulation of their activity by disease and pharmacological drug manipulation. The patch clamp method also allows direct control over the intracellular and the extracellular environment of the target cell via micropipette solution to permit wider experimental setups; for example, effect of specific ionic currents can be isolated by modulating the ionic concentration.<sup>30</sup> However, the number of cells that can be interrogated

simultaneously is limited<sup>31</sup> since this method is inherently tedious and requires precise alignment of the pipette to the target cell under a microscope and adjustment of its proximity and contact with the neuron membrane. In the in-vivo setting where alignment within the cortex under a microscope becomes challenging, electrically guided pipette placements to arbitrary neuronal cells in their way have been recently developed, where the impedance can be used as a measure to indicate cell attachment to the pipette.<sup>32,33</sup> Extracellular recordings with macro- and microelectrode arrays enable the long-lasting electrical interrogation of individual and multiple cells in spatially extended networks. However, the amplitudes of extracellular potentials measured with extracellular electrodes are typically less than a millivolt, and extracellular measurements are insensitive to subthreshold oscillations such as postsynaptic potentials (PSPs).<sup>34</sup> Thus, a technology that could provide the subthreshold dynamics of patch clamp with the spatial resolution of extracellular recording would be of tremendous utility for understanding neural network dynamics.<sup>35</sup>

Over the last decade, the nanowire (NW) interface emerged as a scalable and minimally destructive technology which allows

permeation to neuronal cell membranes for recording at high spatio-temporal resolution.<sup>34,36–43</sup> Some of these studies demonstrated that intracellular NW electrodes can measure intracellular potentials with magnitudes over 70 mV<sup>44–46</sup> which are comparable to that of patch clamp. The minimally invasive nature of the NW electrode was demonstrated by inserting a NW to a whole-cell patched cardiomyocytes (CMs) where the recorded action potentials were minimally altered upon the NW insertion.<sup>44</sup> Despite its advantages, NW technology has its limitations, particularly in maintaining a reliable NW-neuron interface over time. This challenge arises from the fact that the plasma membrane of the cell tends to reject the foreign material and reconstruct the cell membrane, which eventually isolates the NW from the cell body.<sup>47,48</sup> Once the NW is outside the neuron, the recording can no longer be considered intracellular, but rather extracellular.<sup>39</sup>

To gain insight into the advantages and limitations of these three techniques—patch clamp, extracellular, and NW recording—basic circuit models that incorporate relevant charge-transport are used. Figure 2(a) shows the fundamental model for a typical pipette-based



**FIG. 2.** Comparison of (a) patch clamp, (b) extracellular, and (c) NW recording methods in terms of (left) simplified circuit models, (center) microscope images of electrode-neuron interface, and (right) typical recording results. Edited and reprinted with permission from Akita *et al.*, "Patch-clamp techniques: General remarks," in *Patch Clamp Techniques* (Springer, 2012), pp. 21–41. Copyright 2012 Springer Nature.<sup>27</sup> Reprinted with permission from Steriade *et al.*, *J. Neurophys.* **85**(5), 1969 (2001). Copyright 2001 American Physiological Society. Reprinted with permission from Fong *et al.*, *Nat. Comm.* **6**(1), 1 (2015). Copyright 2015 Macmillan Publishers Ltd. Edited and reprinted with permission from Seidel *et al.*, *Analyst* **142**(11), 1929 (2017). Copyright 2017 the Royal Society of Chemistry. Edited and reprinted with permission from Liu *et al.*, *Nano Lett.* **17**(5), 2757 (2017). Copyright 2017 American Chemical Society.<sup>46</sup> Edited and reprinted with permission from Liu *et al.*, *Adv. Func. Mat.* 2108378 (2021). Copyright 2021 IEBL.<sup>74</sup>



measurement of the membrane potential of neurons. Most commonly, the recording electrode consists of a silver/silver-chloride (Ag/AgCl) wire which is a non-polarizable electrode, whereby a large current can pass through the electrode without creating or causing an appreciable potential drop at the electrode-solution interface. The electrode is immersed in an electrolyte solution with precisely controlled ionic concentrations that match the intracellular environment of the neuron.<sup>26</sup> The sub-micron aperture of the pipette tip is used to form a light seal on the lipid membrane (“cell-attached”), during which extracellular currents can be measured. At this point, the membrane can be ruptured through mechanical, chemical, or electrical means to gain “whole-cell” access and ionic exchange with the cytoplasm. In other experiments, the plasma membrane can be pulled away and resealed along the tip of the pipette, providing access to a single ion channel. Ion flow is constricted by the cross-sectional area of the pipette and is effectively modeled by a resistance,  $R_p$ . The sealing resistance,  $R_{seal}$  represents the tight pipette-cell junction, and any associated current leaks out of this seal to the extracellular medium. With the proper amplifier configuration, this method is amenable to measuring absolute membrane potentials. A major advantage to this method is the “clamp,” achieved through the giga-ohm seal that allows the experimenter to manipulate the resting membrane potential or current flow and measure resulting changes in current or voltage, respectively. This capability comes at the cost of low spatial resolution and relatively short recording period of usually under 30 min.

While patch clamp recordings can provide fine resolution of dynamics within a single neuron, it cannot effectively resolve network activities. Instead, researchers employ extracellular electrodes to study activity at a lower dynamic resolution but over a greater area.<sup>49</sup> Figure 2(b) shows a general model for a microelectrode, which can provide insights into the dynamics of neural populations.<sup>50</sup> The large membrane impedance attenuates the signal amplitude in this configuration due in part to the corresponding voltage drop across the impedance of the membrane. Without a highly scaled electrode of a comparable size to that of an individual neuron, and without excellent alignment between the two, the coupling efficiency of neuronal potentials to the electrode can significantly decrease, particularly with electrodes that exhibit large electrochemical impedances.<sup>51</sup> Thus, this system cannot achieve comparable coupling coefficients to that of patch clamp measurements. However, the non-invasive nature of the extracellular approach allows greater chronic compatibility as cells or brain slices can be cultured on these arrays and data can be acquired over days or weeks.

Figure 2(c) shows a general model for a penetrating (impaling through cellular plasma membrane to access intracellular cytosol)<sup>52</sup> NW electrode that forms an interface with the intracellular fluid of the cell. Depending on the electrochemical interface and the recording electronics, the NW interfaces hold the promise of measuring intracellular potentials in a comparable amplitude and signal-to-noise ratio to patch clamp<sup>45</sup> with high spatiotemporal resolution as good as the extracellular microelectrode array.<sup>35,46</sup> The fundamental circuit model that depicts the NW’s neuronal interface is comparable to that of the patch clamp. However, the wire-cytoplasm electrochemical junction usually exhibits a larger impedance for the nanoelectrode compared to that obtained with patch clamp. These effects will be delineated by circuit simulations in the forthcoming discussions in Sec. IV.

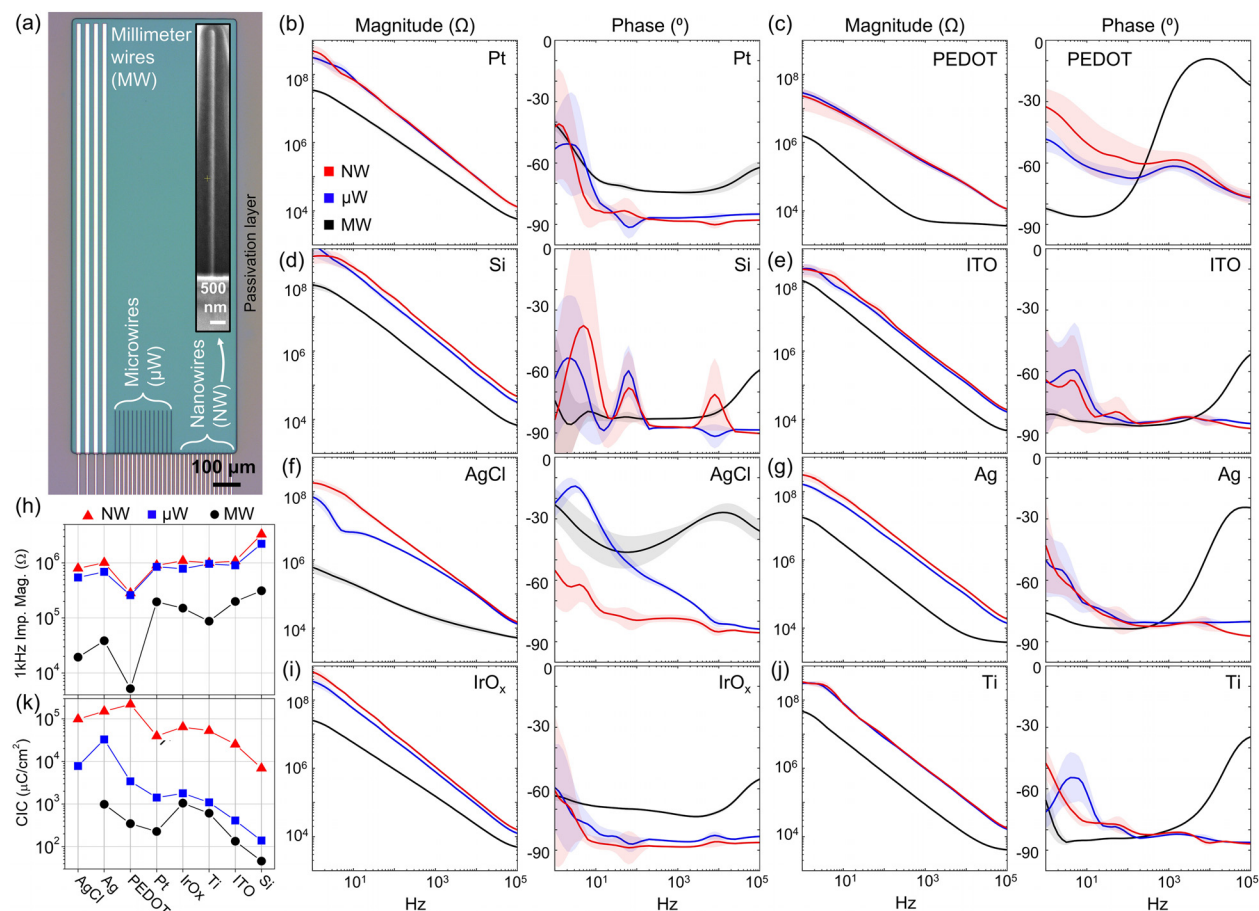
Figures 2(a)–2(c) also illustrate characteristic recording signals from whole-cell patch clamp, extracellular, and intracellular NW

electrodes, respectively. As shown, signals captured by extracellular microelectrodes are smaller in amplitude compared to intracellular recordings obtained by either patch clamp or NW.<sup>35</sup> Patch clamp can record action potentials ( $\sim 100$  mV) and clear subthreshold oscillations together with the absolute membrane potential. Intracellular NWs can reach comparable action potential signal amplitude to that of patch clamp, but the amplitude of recorded potentials in most experiments decreased progressively, eventually becoming comparable to small extracellular potentials.<sup>35,39,43,47,53,54</sup> This is in part due to the temporary permeation of the neuronal cell membrane by electroporation and subsequent rapid repair of the membrane within tens of seconds around the NW.<sup>45,47</sup> Naturally internalized NWs, such as ultrasharp NW (USNWs)<sup>46</sup> or nanostructures with sharp edges,<sup>55</sup> are reported to sustain intracellular access over extended durations of time with a capability to record large action potential amplitudes and subthreshold oscillations without electroporation. These results are further corroborated by more recent experimental studies reported in Secs. V and VI.

### III. ELECTROCHEMICAL CHARACTERISTICS OF ELECTRODES ACROSS MATERIALS AND LENGTH SCALES

The electrode impedance is one of the most critical parameters of bio-interface electrodes that determine the efficacy of a measurement made from a given neuronal activity.<sup>56–60</sup> Although intracellular NWs made from many different interface materials,<sup>44,46,47,61</sup> such as Si, Pt, iridium oxide ( $\text{IrO}_x$ ), and indium tin oxide (ITO), have previously been reported, the detailed electrochemical characteristics of these interface materials at the microscale and the nanoscale have not been established. In Fig. 3, we report the results of electrochemical impedance spectroscopy (EIS) measurement with the interface of NW, microwire ( $\mu\text{W}$ ), and millimeter wires (MW) composed of different interface materials including Pt, Poly(3,4-ethylenedioxythiophene)-poly(styrenesulfonate) (PEDOT:PSS), Ti, Si, Ag, Ag/AgCl,  $\text{IrO}_x$ , and ITO, in a Dulbecco’s phosphate buffered solution (DPBS). Electron beam lithography was used for the precise and uniform patterning of planar NWs,  $\mu\text{W}$ s, and MWs with width  $\times$  length dimensions of  $170\text{ nm} \times 10\text{ }\mu\text{m}$ ,  $1\text{ }\mu\text{m} \times 100\text{ }\mu\text{m}$ , and  $10\text{ }\mu\text{m} \times 1\text{ mm}$ , respectively, as shown by the optical and electron microscope images [Fig. 3(a)]. To ensure uniform current spreading under the intended electrode interface, a 100 nm thick Pt layer was deposited. The interface material was subsequently sputtered (100 nm thick Ag, Ti, and ITO; 5 nm thick  $\text{IrO}_x$ ) or electrochemically deposited (50 nm thick PEDOT:PSS) on top of the Pt. The Ag/AgCl electrodes were fabricated by chlorinating the surface of Ag with a  $\text{FeCl}_3$ -poly(vinylpyrrolidone) (PVP) solution.<sup>62</sup> Si NWs were prepared by the top-down etching of a highly doped silicon-on-insulator (SOI) wafer (device layer: n-type, 220-nm-thick,  $2 \times 10^{20}\text{ cm}^{-3}$ ). To minimize the parasitic capacitance of the metal leads with the underlying carrier substrate, we fabricated the NWs on an insulating 1- $\mu\text{m}$ -thick  $\text{SiO}_2$ -coated Si substrate. A 2- $\mu\text{m}$ -thick AZ1529 photoresist layer was deposited to hermetically seal and passivate the 5  $\mu\text{m}$  wide and 10/100 nm thick Cr/Au metal leads that connected each electrode to the external characterization circuitry.

For all materials under consideration, as the electrode size decreased, the interfacial surface area naturally decreased, and the electrochemical impedance increased, as expected [Figs. 3(b)–3(h)]. The NW electrodes showed predominantly capacitive behavior, evident by



**FIG. 3.** Electrochemical characteristics of the NWs,  $\mu$ Ws, and MWs for different materials. (a) Optical and electron microscope images of the electrodes. Electrochemical impedance spectroscopy of (b) Pt, (c) PEDOT:PSS, (d) Si, (e) ITO, (f) Ag/AgCl, (g) Ag, (i) IrO<sub>x</sub>, and (j) Ti NW,  $\mu$ W, and MW, showing the magnitude and phase of the impedance spectra. (h) 1 kHz impedance magnitude and (k) CIC of wires with different materials.

the  $1/f$  dependence of the impedance magnitude with frequency which was also dependent on the electrode interface material. All MW electrodes except the AgCl electrode show transitions from capacitive to resistive behavior with frequency. The resistive behavior at higher frequencies is attributed to the contributions from the solution and metal-lead resistive components, as well as the current-crowding resistance at the edge of the contacts.<sup>63</sup> For the AgCl MW electrode [Fig. 3(f)], the resistive components dominate the EIS spectra. Further analysis of the electrode through cyclic voltammetry (CV) reveals the formation of Ag complexes close to the equilibrium potential. Consequently, the determination of an accurate charge injection capacity (CIC) for Ag MW electrode was challenging.

PEDOT:PSS is an important organic electrode material due to its permeability of ions that provides it with the unique, volumetric sensitivity of electrophysiological signals, contrasting from typical surface sensitivity of solid-state electrodes.<sup>64–66</sup> Figure 3(c) exhibits the impedance magnitude and phase spectra of PEDOT MW,  $\mu$ W, and NW electrodes fabricated by electrochemical deposition of EDOT molecules on Pt contacts. It is evident that by changing the interface material from Pt [Fig. 3(b)] to 50 nm thick organic PEDOT [Fig. 3(c)], the

impedance magnitude decreases over the entire frequency range. In the frequency range of interest for physiological activity (1 Hz–10 kHz), the PEDOT MW exhibited 40 times lower impedance than the Pt MW; while PEDOT  $\mu$ W and NW showed four times lower impedance than the Pt  $\mu$ W and NW, respectively. Consequently, PEDOT:PSS  $\mu$ Ws and NWs also exhibited higher CIC values than Pt.

The Si MW,  $\mu$ W, and NW were fabricated on SOI substrates that offer a 220 nm thick single crystal Si “device” layer (with low electrical resistivity of  $6 \times 10^{-4}$  ohm-cm) atop a 1  $\mu$ m-thick SiO<sub>2</sub> layer. The Si MW,  $\mu$ W, and NW all showed the highest impedance magnitudes [Figs. 3(d) and 3(h)], the lowest CIC values [Fig. 3(k)] among all the tested materials with the same dimensions, and exhibited similar EIS characteristics regardless of their size, as shown in Fig. 3(d). They also showed highly capacitive EIS spectra [Fig. 3(d)], which we believe arises due to the capacitive behavior originating from the native oxide formed on the Si surface. ITO MW,  $\mu$ W, and NW showed similar EIS characteristics to Si electrodes but with lower overall impedances, likely due to their lower series resistance [Fig. 3(e)].

Ag wires without chlorination [Fig. 3(g)] did not exhibit the faradaic-like electrode behavior that the AgCl wires did [Fig. 3(f)].

Although the Ag electrodes displayed two times lower impedance compared to Ti electrodes [Fig. 3(j)], the general trend of the EIS curves of Ag and Ti wires was similar. Both the Ag and Ti MWs showed a resistive-like transition above 1 kHz, while their  $\mu$ W and NW were pre-dominantly capacitive above 100 Hz.

$\text{IrO}_x$  MW studied here ( $\text{IrO}_x/\text{Pt}$ , 5/100 nm) showed 1.3 times lower 1 kHz impedance magnitude compared to that of Pt MW [Fig. 3(i)] although a thicker  $\text{IrO}_x$  film is expected to show even lower impedance magnitude.<sup>67</sup> This small difference in EIS characteristics observed between  $\text{IrO}_x$  and Pt MWs became negligible for smaller  $\text{IrO}_x$  and Pt wires; the differences in EIS characteristics between  $\text{IrO}_x$  and Pt  $\mu$ Ws (as well as NWs) were indistinguishable.

1 kHz impedance magnitudes of wires with different materials and dimensions are summarized in Fig. 3(h). MWs showed differences in their EIS characteristics depending on the choice of the interface material. As the dimension of the electrode decreased to  $\mu$ W and NW, the differences in impedance magnitude and phase spectra between the electrodes decreased. These results indicate that for NW electrodes, field-enhancements due to edge effects determine the mechanism for electrochemical interactions, in contrast to the conventional faradaic and capacitive regimes conventionally discussed for larger electrode scales. However, significant differences still emerge between NW electrodes for different materials. For example, the impedance values of PEDOT and Si NWs at 1 kHz were 300 k $\Omega$  and 3 M $\Omega$ , respectively, despite having nearly identical dimensions. Additionally, the faradaic and capacitive behavior of NW electrodes differed significantly for each material. Thus, the choice of the NW material should play an important role in enhancing the coupling coefficient of neuronal activity to the NW. These effects were studied and are summarized in Sec. IV.

Finally, to quantify the stimulation capabilities of these selected materials at various length scales, the CIC of the NW,  $\mu$ W, and MW with different materials is calculated, as shown in Fig. 3(k). The CIC is a measure of the charge density that can be injected through a given electrode before the potential drop across the electrode interface exceeds that of water hydrolysis. To determine the water hydrolysis window, we performed CV measurements for each electrode to determine the water window. For each material and length scale, we injected cathodic first biphasic currents and measured the resulting voltage transients. After obtaining a minimum of 5–8 voltage transients per material and length scale, we extrapolated the voltage transients to intersect with the water hydrolysis values obtained from CV. This corresponding current limit was then divided by the electrode surface area and multiplied by the cathodic pulse duration in order to obtain the CIC limit. The CIC of the MW strongly depended on the interface materials, which agrees well with the previous studies.<sup>68</sup> Additionally, there was a significant increase in the CIC values when the wire dimension was shrunk from  $\mu$ W to NW compared to the relatively small increase in CIC observed when the wire dimension changed from MW to  $\mu$ W. This finding indicates that the geometrical effects that cause strong local fields near the NW surface under relatively high current densities play a significant role in determining CIC value of NW electrodes.

#### IV. THE NANOWIRE-NEURON JUNCTION

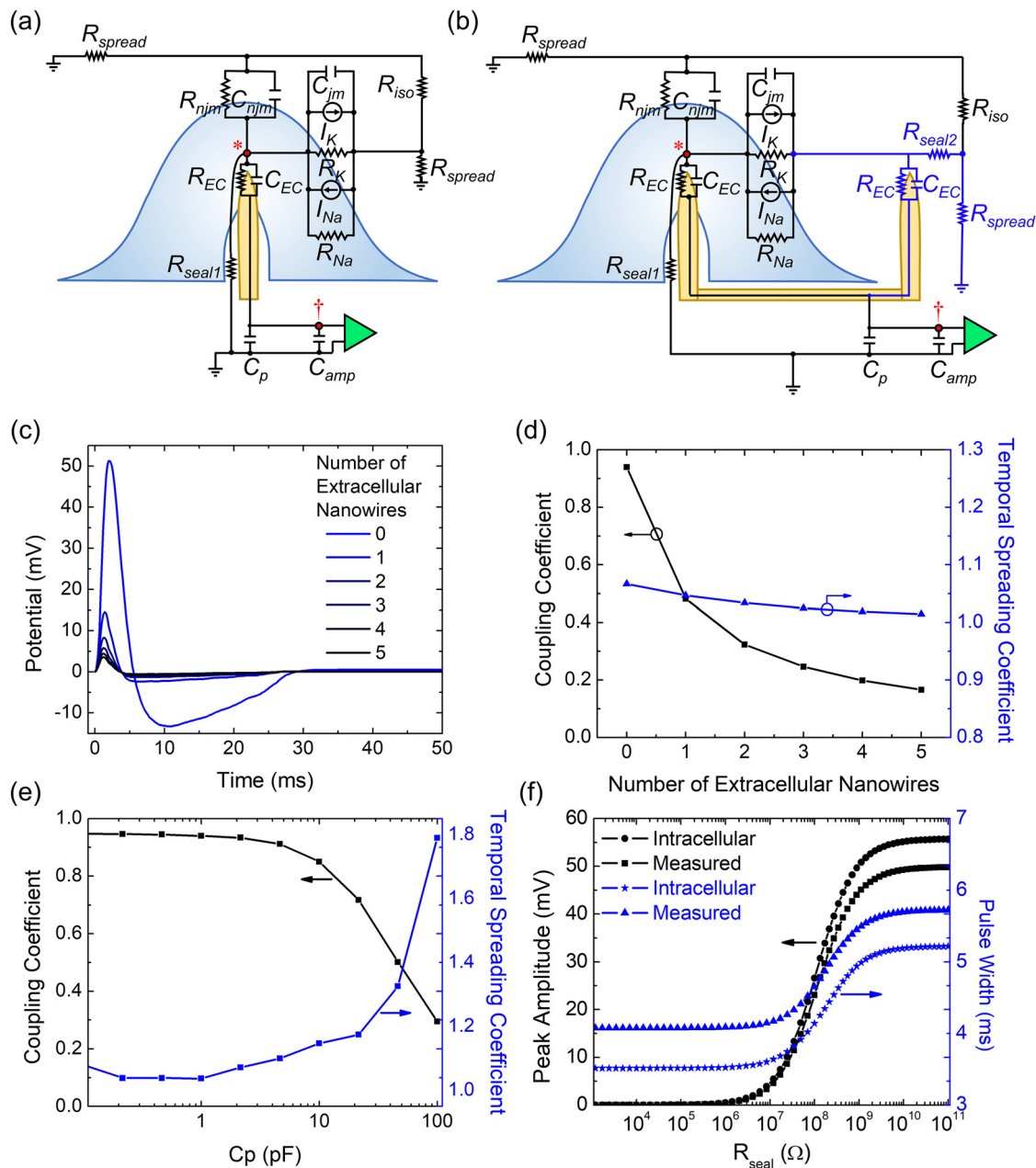
The nature of the geometrical configuration of a NW-neuron interface strongly influences the electrophysiological recordings by

distorting the neuronal signal measured by a recording amplifier.<sup>19,20,36,37,48,61,69</sup> The signal pathways were briefly touched upon in Sec. II and expanded here building off the investigations by Spira and Hai<sup>19</sup> on experimental paradigms in which electrodes with multiple NWs were used.<sup>35,47,70</sup> As illustrated in Fig. 4(a), the neuron is modeled by two lumped membrane impedances. One is active, contributing to ionic current (denoted as a junctional membrane) and the other is passive, depicting leakage across the cellular membrane (denoted as a non-junctional membrane). The ground for this circuit model exists some distance away from the cell, separated by some spreading resistance ( $R_{\text{spread}}$ ) between the outside of the cell and ground. This extracellular impedance is crucial for modeling non-zero potentials outside of the cell, allowing for a reversal in the measured potential polarity which might result from an opposite change in ionic charge polarity at the active membrane junction. This detail is important when considering the effects of a poor membrane seal around a penetrating NW. The electrochemical interface between the intracellular fluid and the intracellular NW is usually modeled as a simple Randles cell which is composed of a parallel RC circuit ( $R_{\text{EC}}$   $C_{\text{EC}}$ ). The quality of the membrane seal around this penetrating electrode is modeled with a sealing resistance  $R_{\text{seal}}$ . Finally, there may exist a signal pathway between the non-junctional extracellular region and the junctional extracellular region. We introduce here an isolation resistance ( $R_{\text{iso}}$ ) to capture this effect.

While extensive prior efforts focused on NW-neuron interfaces with multiple NWs on a single pad,<sup>35,47,70</sup> the impact of the presence of multiple-wires, some inside and some outside the cells, has not been modeled, studied, or discussed in detail before. We illustrate in Fig. 4(b) a situation wherein one NW penetrates the neuron, while the other sits outside. Here, we capture the situation with an extracellular NW that is near a lumped model of the junctional portion of the membrane which contributes to the transmembrane ionic current. One can intuitively deduce that the amplitude of the recorded signals will be attenuated in this latter configuration because the transmembrane potential of the neuron is effectively shorted through the NWs. This intuition is supported by Fig. 4(c), where the simulated potential at the input of the amplifier is plotted for various numbers of extracellular NWs on a single pad. The amplitude of the waveform is largest in the case of a single intracellular NW with zero extracellular NWs shorted on the same pad and decreases as more extracellular NWs are added. Furthermore, in Fig. 4(d), the coupling coefficient, which we define as the ratio of the peak potential seen by the amplifier over the peak intracellular potential, decays exponentially with increasing number of extracellular NWs. We also introduce here a temporal spreading coefficient, which is defined as the ratio of pulse widths of the simulated signal at the input to the amplifier over the intrinsic width of the unperturbed intracellular potential. To the first order, this coefficient can provide insight into the frequency-dependent signal distortion and is shown to decrease with the number of NWs per pad. These simulation results agree well with experimental results that are presented in Fig. 9, which compares electrophysiological recordings from neuro-nal cells using a single NW and multiple NWs on a single pad.

The most critical parameters that can affect the signal seen by the amplifier are the parasitic capacitance ( $C_p$ ),  $R_{\text{seal}}$ ,  $R_{\text{EC}}$ , and  $C_{\text{EC}}$ . Figure 4(e) shows the impact of  $C_p$  on the signal distortion. From Fig. 4(a), one can see that  $C_p$  and  $C_{\text{amp}}$  form an effective capacitive load, which, together with  $R_{\text{EC}}$  and  $C_{\text{EC}}$ , forms a frequency-dependent voltage





**FIG. 4.** Modeling NW-neuron junction. Circuit diagram of (a) single NW penetrating a cell and (b) multiple NWs which are partially engulfed in a cell. Nodes used for \*intracellular and †measured potential are indicated in red color. (c) Simulated action potential at the input of the amplifier plotted for various numbers of extracellular NWs on a single pad. Coupling and temporal spreading coefficients with (d) increasing number of extracellular NWs and (e) parasitic capacitance. (f) Sealing resistance dependent peak amplitude and pulse width of action potential inside the cell and at the input of the amplifier. Reprinted with permission from Liu *et al.*, Adv. Func. Mat. 2108378 (2021). Copyright 2021 IEBL.<sup>74</sup>

divider. Thus, with increasing  $C_p$ , we see a sharp decrease in the coupling coefficient as this load impedance shunts AC signals seen by the amplifier input more strongly toward ground. Thus, Fig. 4(e) shows that  $C_p$  is a critically important parameter that should be minimized for optimal recordings.

The parameter  $R_{seal}$  is another critical part of the NW-neuron interface, and its effect on signal distortion is illustrated in Fig. 4(f). The  $R_{seal}$  component forms a separate signal path to ground which is in parallel to the intracellular electrode's signal path and thus could greatly affect the measured electrophysiological signal. If the value of



$R_{\text{seal}}$  is large compared to other signal paths from inside the cell to ground, then it will produce negligible signal distortion. However, a small  $R_{\text{seal}}$  can be indicative of an ionic conduction path between the extracellular and intracellular mediums. If it approaches similar orders of magnitude to the impedance of the primary signal path (i.e., the electrochemical interfacial impedance), we begin to see a sharp decrease in amplitude at the amplifier input as current is redirected away from the electrode toward this leakage path. In the limit, the amount of current flowing through the electrode becomes negligible compared to this leakage path; thus, the voltage drops across the electrode interface and the intracellular potential across the cell membrane become very small [Fig. 4(f)]. However, this regime where  $R_{\text{seal}}$  is exceptionally low likely indicates a compromised interface where the health of the cell will potentially be compromised as well, and the modeling discussed above will no longer apply.

In order to examine the impact of the electrode impedance (which is composed of  $R_{\text{EC}}$  and  $C_{\text{EC}}$ ) on signal distortion, we performed a parametric sweep of  $R_{\text{EC}}$  and  $C_{\text{EC}}$  following the same circuit diagram in Fig. 4(a) and subsequently calculated the coupling coefficient and temporal spreading coefficient (Fig. 5). Contour lines indicate the log of the magnitude of impedance at 1 kHz, the commonly used frequency that represents the frequency content of an action potential,<sup>71</sup> as a function of  $R_{\text{EC}}$  and  $C_{\text{EC}}$ . Interestingly, Fig. 5(a) clearly demonstrates that two intracellular NW electrodes with similar impedance magnitudes at 1 kHz can have dramatically different coupling coefficients, depending on whether their impedance is Faradaic- or capacitive-dominant. For example, if we have a 1 kHz impedance magnitude between 10 and 100 M $\Omega$  [see the two-way arrow line in Fig. 5(a)], the more Faradaic-like electrodes will likely have a higher coupling efficiency and lower temporal spreading coefficient compared to the more capacitive-like electrodes. An analogous trend is observed for the temporal spreading coefficient [Fig. 5(b)] for electrode impedance over 10 M $\Omega$  at 1 kHz, where larger temporal spreading or signal distortion is generally expected for more capacitive-like electrodes, but the temporal spreading coefficient became near unity for purely capacitive electrodes.

We also estimated the  $R_{\text{EC}}$  and  $C_{\text{EC}}$  parameters for the 10  $\mu\text{m}$  long NWs with different materials from the experimental EIS in the frequency range of 0.1–10 kHz of Fig. 3 and overlaid them on top of

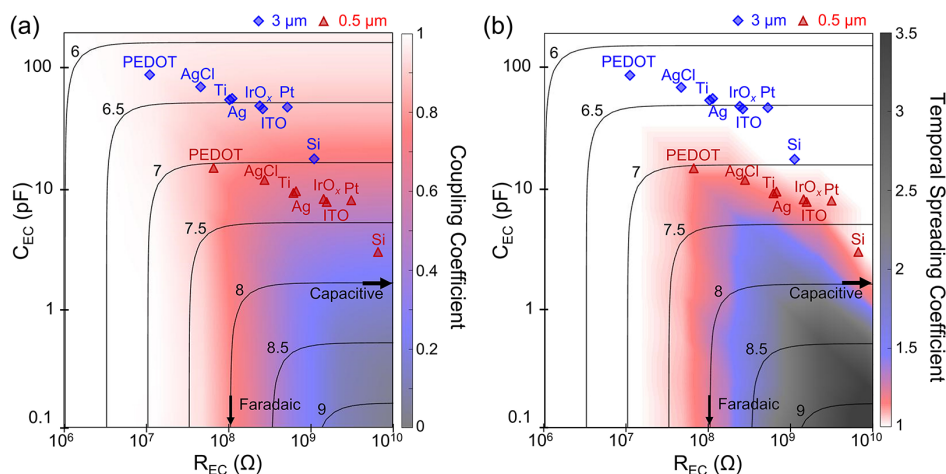
the mapping plot of Fig. 5. We included the ( $R_{\text{EC}}$ ,  $C_{\text{EC}}$ ) of NWs with tip exposure length of 3  $\mu\text{m}$  (blue) and 0.5  $\mu\text{m}$  (red) which we calculated by assuming that the capacitance and resistance are proportional and inversely proportional, respectively, to the length of the NW. Among all the NWs, PEDOT:PSS-coated NW showed the most faradaic-like behavior and is expected to show near unity coupling coefficient even at a 0.5  $\mu\text{m}$  tip exposure. On the other hand, Si showed the highest impedance magnitude among all NWs with the same dimension, and Si with 0.5  $\mu\text{m}$  tip exposure is expected to show a highly attenuated and distorted action potential recording [Figs. 5(a) and 5(b)]. These results indicate that the amplitude and width of action potentials can look considerably different depending on the choice of surface material used for the intracellular NWs.

With these foundational electrochemical aspects of the NW-neuron interface discussed, we next provide a survey of the recent progress in electrophysiological interrogation of nanoscale neuronal interfaces and design considerations that can enhance their fidelity.

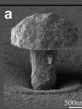
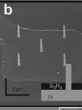
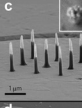
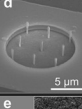
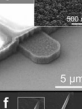

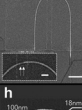
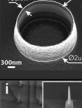
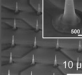
## V. RECENT PROGRESS IN NANOWIRE-NEURON ELECTROPHYSIOLOGICAL RECORDINGS

The endeavor in NW-neuron interfaces is to scale up stable intracellular electrode arrays for neural recording. In order to record intracellular potentials while simultaneously achieving massive scaling and parallelization, current state of the art devices (Fig. 6) have focused on vertical NW electrode arrays and devices to interface with electrically active cells.<sup>43</sup> NW electrodes have allowed easy integration with micro- and nanopatterning techniques, a millisecond temporal resolution, and promising minimal invasiveness with cells based on the geometry and shapes of the electrodes.<sup>36,72,73</sup> The dimensions of the tips of NW electrodes range from sub-10 nm<sup>74</sup> to  $\mu\text{m}$ -scale.<sup>39</sup> They achieve intracellular recordings through combinations of membrane penetration,<sup>46,52,69</sup> electroporation (the application of electric fields above breakdown fields of the cellular membrane),<sup>47,54</sup> optoporation (laser-induced intracellular access),<sup>55</sup> and/or proper cellular engulfment.<sup>39</sup>

One of the most prominent  $\mu\text{m}$ -scale vertical electrodes are the gold mushroom-shaped microelectrode (gM $\mu\text{E}$ ) pillar arrays, developed by Hai *et al.*,<sup>53,75</sup> which are individually addressable. Standard photolithography and electroplating methods are used to fabricate gM $\mu\text{E}$  arrays composed of 60 individual pillars. The gM $\mu\text{E}$ s are



**FIG. 5.** Mapping of the (a) coupling and (b) temporal spreading coefficients depending on the  $R_{\text{EC}}$  and  $C_{\text{EC}}$  of the NW electrode.  $R_{\text{EC}}$  and  $C_{\text{EC}}$  values of NWs with different materials were estimated from the electrochemical impedance spectroscopy and plotted on top of the mapping plot. NWs with tip exposure length of 3  $\mu\text{m}$  (blue) and 0.5  $\mu\text{m}$  (red) are plotted in different colors and symbols.

	Key Electrode Device Figure	Number of vertical electrodes (nanowires) per cell	Electrode			Channel count	Fabrication Process	Cell-electrode Interface formation method	Passivation layer / cell culture surface material	Studied cell types	Recording				Ref.	
			Surface material	Effective interaction dimension	Impedance						Coating	Coupling coefficient	Max AP (mV)	Max EPSP		Duration of stable recording
Gold mushroom (GM $\mu$ E)		1	Au	1 $\mu$ m	100 G $\Omega$	RGD repeat peptide Poly-L-lysine	64	Electroplating	Engulfment and electroporation	SiO <sub>2</sub>	Aplysia, rat hippocampal cells, NIH/3T3, CHO CM, PC-12, H9C2	$\sim$ 0.1 – 0.5	Aplysia: $\sim$ 2 – 30	Aplysia: $\sim$ 5 mV	5 min after electroporation Stable interface w/ Aplysia, max 2 weeks	[19], [53]
Pt nanopillars		1 - 10	Pt	150 – 200 nm per wire	$\sim$ 5 – 19 M $\Omega$ @ 1 kHz	Fibronectin in gelatin	16 / 60	FIB-assisted Pt deposition	Electroporation	Si <sub>3</sub> N <sub>4</sub> /SiO <sub>2</sub>	HL-1 mouse CM, hESC-CM, hiPSC-CM	$\sim$ 0.1 / 0.25	$\sim$ 12 / 25	None	10 min	[47], [77]
Pt nanoneedles on CMOS		9	Pt / Pt black	100 nm per wire / $\sim$ 500 nm per wire	$\sim$ 100 M $\Omega$ @ 1 kHz / 300k $\Omega$ @ 5kHz	No coating	1024 / 4096	Top down etching and electroplating	Electroporation	SiO <sub>2</sub>	Primary rat cortical neurons / Neonatal rat ventricular CM	$\sim$ 0.1 / $<$ 0.2	$\sim$ 10 / $\sim$ 20	$\sim$ 500 $\mu$ V / None	8 min Max: $\sim$ 19 min	[35], [54]
3D Plasmonic Hollow Nanocylinder		9 - 25	Au	$\sim$ 150 nm per nanocylinder	Not reported	Poly-dl-ornithine	24	FIB-assisted Ion milling	Optoporation	SU-8, SiO <sub>2</sub> , Polyimide	Rat hippocampal cells, HL-1 mouse CM	$\sim$ 0.02	$\sim$ 2	None	80 min	[55]
3D Fuzzy Graphene		1	Graphene	$\sim$ 25 $\mu$ m <sup>2</sup> to 2500 $\mu$ m <sup>2</sup>	0.01 – 1 M $\Omega$ @ 1 kHz	Fibronectin	24	PECVD-based bottom-up growth	Optoporation	SU-8	hiPSC-CM, HL-1 mouse CM	$\sim$ 0.06	$\sim$ 6	None	20 min	[79]
Branched intracellular nanotube FET		1	Si	50 – 55 nm	FET Device	Phospho-lipid	3 multiplexed devices	Bottom up growth	Mechanical insertion or spontaneous	PDMS	Embryonic chicken CM	$\sim$ 1	100	None	1 hour	[69]
U-shaped nanowire FET		1 – 4	Si	15 nm	FET Device	Phospho-lipid	$\sim$ 10 multiplexed devices	Controlled dispersion	Mechanical insertion or spontaneous	PDMS	DRG neurons, HiPSC CM	$\sim$ 1	$\sim$ 60 – 100	$\sim$ 5 mV	DRG: $\sim$ 150 s max HiPSC CM: $\sim$ 900 s max	[45]
Nanovolcano		1	Pt, Au	100 nm	1.3 G $\Omega$	Alkanethiol self-assembled monolayers	21 – 28	Top down etching and sputtering	Natural internalization and electroporation	SU8	Neonatal rat ventricular CM	$\sim$ 0.6	62	None	66 min	[82], [83]
Ultra-sharp nanowire array		1	Si / Pt	100 – 200 nm / $<$ 10 nm	$\sim$ 20M $\Omega$ @ 1 kHz	No coating	64	Top down etching	Natural internalization	Plasma treated parylene-C/ SiO <sub>2</sub>	CA1-CA3 rodent primary neurons, hiPSC-derived neurons / iPSC-derived CM	$\sim$ 1 / $\sim$ 0.1	99 / 13	1 mV*	$\sim$ 6 min	[46], [74]

**FIG. 6.** Structures, specifications, fabrication methods, and recording capabilities of current state of the art nano- and microelectrodes. Reprinted with permission from Spira *et al.*, *Front. Neurosci.* **12**, 212 (2018). Copyright 2018 Frontiers Media S.A.<sup>75</sup> Reprinted with permission from Xie *et al.*, *Nat. Nanotechnol.* **7**, 185 (2012). Copyright 2012 Macmillan Publishers.<sup>47</sup> Edited and reprinted with permission from Abbott *et al.*, *Nat. Nanotechnol.* **12**, 460 (2017). Copyright 2017 Macmillan Publishers.<sup>54</sup> Edited and reprinted with permission from Abbott *et al.*, *Nat. Biomed. Eng.* **4**, 232 (2020). Copyright 2020 Macmillan Publishers.<sup>35</sup> Reprinted with permission from Dipalo *et al.*, *Nano Lett.* **17**, 3932 (2017). Copyright 2017 American Chemical Society.<sup>55</sup> Edited and reprinted with permission from Dipalo *et al.*, *Sci. Adv.* **7**, eabd5175 (2021). Copyright 2021 AAAS.<sup>79</sup> Reprinted with permission from Duan *et al.*, *Nat. Nanotechnol.* **7**, 174 (2012). Copyright 2012 Macmillan Publishers.<sup>69</sup> Reprinted with permission from Zhao *et al.*, *Nat. Nanotechnol.* **14**, 783 (2019). Copyright 2012 Macmillan Publishers.<sup>45</sup> Reprinted with permission from Desbiolles *et al.*, *Nano Lett.* **19**, 6173 (2019). Copyright 2019 American Chemical Society.<sup>82</sup> Edited and reprinted with permission from Liu *et al.*, *Adv. Func. Mat.* 2108378 (2021). Copyright 2021 IEBL.<sup>74</sup>

non-invasive, extracellular microelectrodes that the cell membrane can properly engulf to achieve “in-cell”-like recordings of intracellular potentials from cultured neurons, primary CMs, striated muscle fibers, and non-excitable cells (3T3, CHO, PC-12, H9C2). The unique shape of the gMμEs essentially mimics the shape, structure, and dimension of neuronal dendritic spines to compel a cell to naturally engulf an electrode.<sup>39</sup> With additional chemical functionalization by R 1/4 arginine, G 1/4 glycine, D 1/4 aspartic acid, and a long decalysine (K) 10 spacer (RGD) repeat peptide or laminin, phagocytic engulfment was further improved. Similar to other state of the art electrode devices, a short electroporation pulse via gMμE allowed similar in-cell

recordings for contracting CMs and striated muscle fiber cells under *in vitro* conditions; the action potential signal amplitude varied from 5 to 10 mV. While earlier studies used μm-scale gMμE electrodes to record electrophysiological activity from relatively larger cells, such as non-mammalian Aplysia neurons and CMs, recent gMμE have interrogated smaller and more challenging mammalian neuron (primary rat hippocampal neuron) cultures with excellent recording results that showed more than 90% monophasic positive action potentials with recorded potential amplitudes of up to 5 mV.<sup>76</sup>

Xie *et al.*<sup>47</sup> and Lin *et al.*<sup>77</sup> have also utilized electroporation to achieve intracellular recording of action potentials. Electroporation is

very effective in temporarily breaking the cell membrane by a large electric field to access the intracellular medium to measure intracellular action potentials. This general method works well for NWs,<sup>35,47</sup>  $\mu$ Ws,<sup>76</sup> and even planar electrodes<sup>78</sup> that could not naturally permeate the cell membrane. They specifically used  $3 \times 3$  and  $4 \times 4$  platinum (Pt) pad arrays where each pad contained nanopillar structures with sub-100 nm tips. The nanopillars were fabricated using focused ion beam (FIB)-assisted Pt deposition and approximately 1–10 NWs were formed on the Pt pads; the NWs within the same pad were thus not individually addressable. With nanoscale electrode tips and nanoscale electroporation, a large electric field temporarily breaks the membrane to permeate or provide access of the intracellular medium to the NWs and facilitates measurements of intracellular action potentials of HL-1 CM, human embryonic stem cell derived CM (hESC-CM), and human-induced pluripotent stem cell-derived (hiPSC)-CM cell cultures. The electroporation essentially allowed manual switching from extracellular to intracellular recordings. After the nanopillar electrodes delivered electroporation pulses, the intracellular signal amplitude increased to 11.8 mV compared to the immediately prior measured extracellular amplitudes of 100–200  $\mu$ V.<sup>47</sup> However, 120 s after the electroporation pulse, the signal amplitude decayed to 30% and the signal returned to extracellular characteristics after 10 min.<sup>47</sup> The intracellular measurements were demonstrated on relatively larger type of CMs, similar to initial studies with gM $\mu$ E.

Abbott *et al.*<sup>35,54</sup> have utilized complementary metal-oxide semiconductor (CMOS) acquisition circuits built directly under the NW arrays to achieve massive parallelization of 4096 simultaneous recording and stimulation sites: the system was named CMOS neuroelectronic interface (CNEI). Each of the 4096 recording sites (array of  $64 \times 64$  aluminum pads) contains nine Pt-black electrodes, which were fabricated precisely to have approximately 300 k $\Omega$  impedance. By coating Pt-black with characteristic surface roughness on Pt nanoneedles via electrodeposition, not only the surface area of the electrode was increased but also its characteristic electrochemical activity, so much so that the CIC also increased. With a greater CIC, water hydrolysis was prohibited, and micrometer-scale gas bubble formations were eliminated providing more reliable electroporation for intracellular access. During a recording session on rat neurons *in vitro* (combined from cortex, hippocampus, and ventricular regions), 1837 sites showed parallel intracellular recording; in a separate 19 min recording/stimulation session, 1728 sites were observed to be recording in parallel, and up to 982 sites showed simultaneous intracellular coupling.<sup>35</sup> The CNEI demonstrated a platform to allow simultaneous measurements of subthreshold membrane potentials from many different neurons and facilitated characterization of neuron signal pathways and synaptic connections.

Other than electroporation, optoporation has also been used as an alternative strategy to gain intracellular access. Dipalo *et al.* have utilized laser irradiation on Au<sup>55</sup> and graphene<sup>79</sup> electrodes to generate hot carriers through surface plasmon polaritons. When a critical number of hot electrons are generated and thereby produce even more electrons through a cascade of impact ionization, the rapid increase in the kinetic momentum of water molecules surrounding the electrode causes nano-shockwaves. These mechanical waves consequently induce nano-bubbles that disrupt the cell membrane to allow three-dimensional (3D) electrodes to gain intracellular access.<sup>80</sup> For hot electron generation through excitations of surface plasmon polaritons, Dipalo *et al.* fabricated Au hollow nanocylinders with diameter of

150 nm and height of 1.8  $\mu$ m through FIB-assisted ion milling by producing solvent-insoluble polymer at the milled surface and subsequent Au coating.<sup>55,81</sup> Recordings were performed with rat hippocampal neurons and HL-1 cardiac cells. Following selective optoporation of nanocylinder in proximity with the target cell with laser focused on the tip of the electrode, a transition from extracellular to intracellular interface was accomplished.<sup>55</sup> Thus, intracellular action potentials, up to approximately 2 mV in amplitude, were recorded over a duration of 80 min.<sup>55</sup> Recently, 3D, rectangular-shaped (relatively larger:  $5 \times 5$ – $50 \times 50$   $\mu$ m<sup>2</sup>) fuzzy graphene-based electrode was also demonstrated to record intracellular action potentials (up to 6 mV in amplitude and 20 min of recording from hiPSC-CMs and HL-1 cardiac cells) following direct optoporation treatment with ultrafast pulsed laser in the near-infrared regime.<sup>79</sup> The laser irradiation was deemed to not be detrimental to the cells for both types of electrodes.<sup>79</sup> The parallel recording for both types of electrodes was conducted on 24 channels. The integration of nanotubes on hundreds of CMOS micro-electrode array (CMOS-MEA) was specifically demonstrated together with intracellular action potential recordings.

Duan *et al.*<sup>69</sup> and Zhao *et al.*<sup>45</sup> have focused on the structure and geometry of their NW devices and additional chemical modifications to gain minimally invasive access to the cell membrane, namely, nanoscale field-effector transistor (FET)-based intracellular measurements. Duan *et al.* initially integrated SiO<sub>2</sub>-based nanotube (inner tip diameter of 50 nm and outer tip diameter of 55 nm) on top of a nanoscale FET.<sup>69</sup> The branched intracellular nanotube FET (BIT-FET) mechanically penetrates the cellular membrane to expose the cellular cytosol to the FET p-type Si NW channel to measure intracellular transmembrane potential. BIT-FET successfully recorded intracellular potentials from embryonic chicken CMs.<sup>69</sup> Continuing from this work, Zhao *et al.* developed ultra-small NW probes for intracellular interrogation.<sup>45</sup> With an appropriate nanoscale curvature on the cell membrane, they recorded intracellular potentials from primary rat dorsal root ganglion neurons and hiPSC-CMs cultures. The device is essentially a U-shaped Si NW FET with a specific radius of curvature made from 15 nm diameter Si NW. The conductance of the Si layer located at the tip of the device can be modulated by ionic potential fluctuations which in a transistor with proper potential bias can lead to amplified sensitivity to these electrophysiological potentials. Immediately adjacent to the nanoscale Si region of the inserted NW device is a locally formed silicidic alloy (NiSi) that established the source and drain contacts to the Si NW and is accomplished with Ni diffusion into the Si NW via rapid thermal annealing. Zhao *et al.* reported that these electrodes have potential to multiplex 168 channels.<sup>45</sup> Both the SiO<sub>2</sub> nanotube FET and U-shaped Si NW FET were treated with phospholipid chemical modification to enable nearly full amplitude intracellular recordings ranging from 75 to 100 mV and 60 to 100 mV, respectively.<sup>45,69</sup>

Desbiolles *et al.* achieved intracellular recordings through relatively new “nanovolcano” microelectrode.<sup>82,83</sup> The nanovolcano structure is composed of nanopatterned SiO<sub>2</sub> cylinder shaped in a three-dimensional “volcano” structure, a Ti-Au-Ti layer, and a Pt internal wall/surface. The 10–20 nm Au layer in between the nanovolcano multi-layers and the high-curvature of the wall itself increased the probability of intracellular access into the target cell.<sup>82</sup> As with many aforementioned devices, nanovolcano exhibited temporary intracellular access through electroporation and achieved a recording yield of around 76% of nanovolcano channels and recording fidelity of up to



62 mV from neonatal rat CMS.<sup>83</sup> Notably, nanovolcano also displayed natural access into the CMs without controlled electroporation with a maximum recording yield around 30% of channels and maximum amplitude of around 20 mV.<sup>82</sup> Nanovolcano with no intentional electroporation treatment demonstrated more than one hour of stable intracellular recording, and with additional electroporation, recording duration could potentially be increased further up to total of 75 min.<sup>82</sup> While electroporation allowed higher recording yield and amplitude, amplitude and recording duration decreased with each successive electroporation, and after four repeated applications of electroporation, the nanopatterned nanovolcano ceased to record intracellular activity.<sup>83</sup>

We focused on obtaining natural intracellular access into neuronal cells through the development of relatively longer ( $\sim 7\ \mu\text{m}$ ) vertical and individually addressable NW arrays.<sup>46,74</sup> These were initially fabricated with the Si interface that recorded intracellular potentials from cultured rodent primary neurons and human induced pluripotent stem cells. The NWs were fabricated by using a combination of photolithography and e-beam lithography techniques, and essential reactive ion etch to form a high aspect ratio NW structure. To achieve lead-to-lead electrical isolation for individual electrical addressability of the NW array, NiSi alloy was formed to bond on Si substrates to Ni patterned, insulating sapphire substrates.<sup>46</sup> All materials except for the Si NW tips were coated with insulating  $\text{SiO}_2$  dielectrics for passivation to prevent electrochemical transduction except for the Si tips. The tall and sub-100 nm tip diameters of the vertical NW structures afforded natural intracellular recordings with high signal to noise ratios, and sensitivity to detect subthreshold PSPs was revealed; the measured potentials varied from 0.1 to 99 mV.<sup>46</sup>

## VI. FABRICATION METHODS FOR INTRACELLULAR NANOWIRES

As introduced in previous discussion, achieving a precise morphology-controlled nanostructure is the key for obtaining intracellular access to the cells, which would in turn determine the amplitude and quality of electrophysiological signals. As illustrated in Fig. 7, numerous fabrication approaches were used to make nanostructures with controlled morphologies and dimensions that are optimal for intracellular recording. One important fabrication parameter to consider when integrating NWs with acquisition circuits is the temperature of the integration process to prepare the NWs. A high process temperature could be detrimental to the metal leads or passivation layers in the circuits, as well as the impurity doping profiles for any transistor components, which is especially critical in scaled CMOS technology with small features. In this regard, the fabrication processes that involve the high temperature ( $>400^\circ\text{C}$ ) is indicated by coloring the substrates with red in Figs. 7(a)–7(d). For the NWs prepared under high temperature processes, the metal leads to address individual NWs are usually formed after the NW preparation steps.

Anisotropic or directional etching is one of the most widely used methods to fabricate high aspect ratio nanostructures [Fig. 7(a)]. With plasma etching masked by small metal dots that are smaller than  $1\ \mu\text{m}$  in diameter, nearly any planar material with a few  $\mu\text{m}$  thickness could be transformed into NWs.<sup>46,61,84</sup> Alternatively, anisotropic wet etching can create high aspect ratio NWs from single crystal substrates,<sup>85,86</sup> and patterned Ag or Au metal layers can be used to control the shape and position of nanostructures using so-called “inverse metal-assisted chemical etching.”<sup>87,88</sup> Additionally, the diameter of NWs prepared by

directional etching methods could be further thinned down by isotropic etching process [Fig. 7(a)]. For example, reactive ion etching followed by wet etching process enabled the fabrication of amorphous- $\text{SiO}_2$  NWs with a height and a diameter of  $3\ \mu\text{m}$  and 100 nm, respectively.<sup>61</sup>

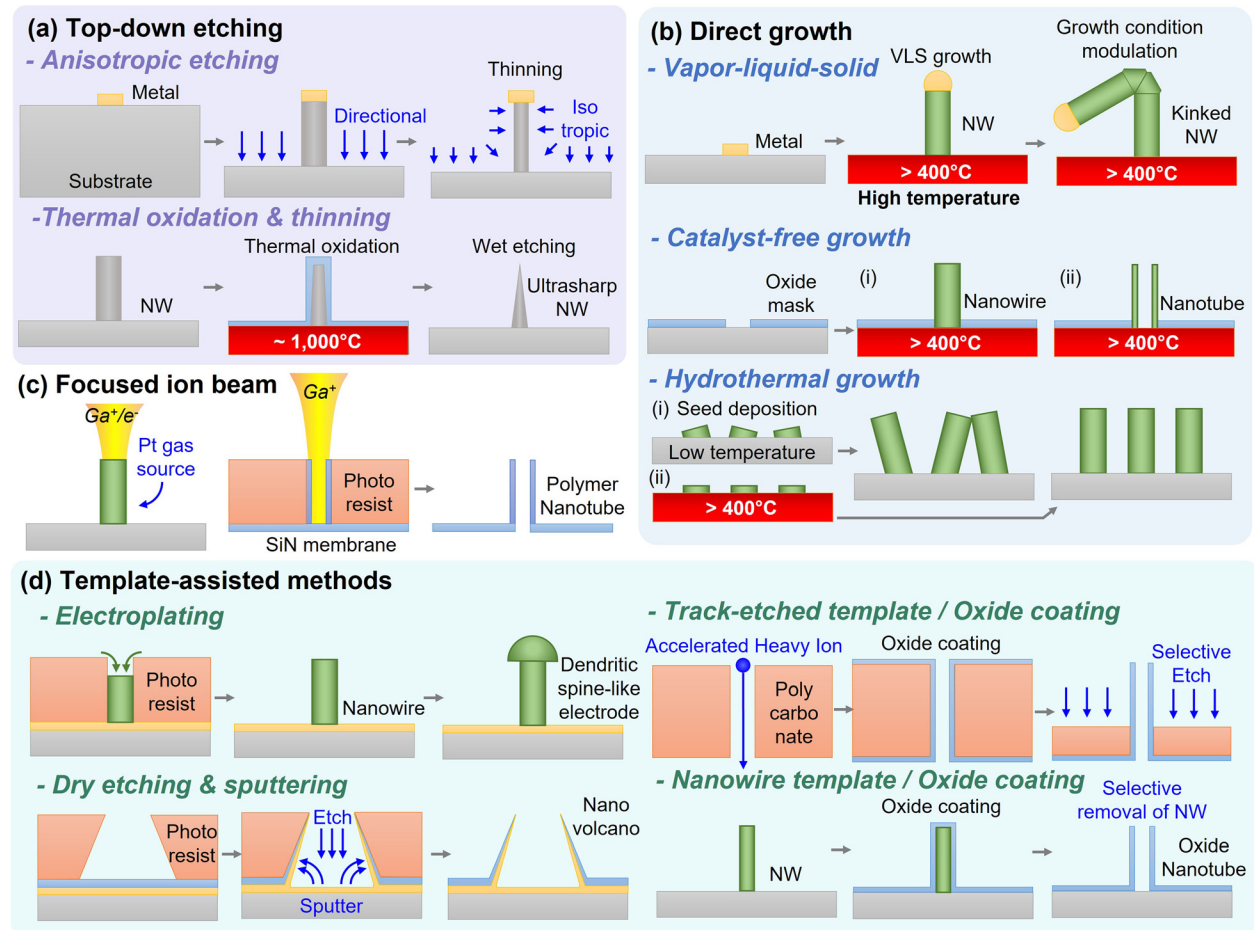
However, for the fabrication of taller NWs ( $>7\ \mu\text{m}$ ) with smaller diameter tips, the starting material's structural integrity and stiffness become increasingly important. For this reason, instead of relying on polycrystalline materials such as  $\text{SiO}_2$ ,  $50\ \mu\text{m}$  thick single crystal Si was bonded on top of the predefined metal leads on a transparent sapphire substrate via nickel silicide bonding method.<sup>89</sup> The bonded Si was further thinned to  $7\ \mu\text{m}$  with unmasked dry etching, and utilizing electron beam lithography to align Ni mask dots atop the underlying metal leads and a controlled etching process, high aspect ratio,  $7\ \mu\text{m}$  tall NWs with diameters as small as 60 nm were formed.<sup>46</sup>

Precise thinning of the NW tip diameter is a crucial process to increase the probability of NWs to naturally internalize the cell membrane.<sup>52,90</sup> As discussed above, additional isotropic etching process can be applied to thin down the diameter of the NWs. Sharpening the tip of the NWs can be accomplished by employing thermal oxidation method that diffuses  $\text{O}_2$  into the Si surface at  $\sim 1000^\circ\text{C}$  [Fig. 7(a)]. This Angstrom level control of  $\text{SiO}_2$  layer thickness, wet etching of  $\text{SiO}_2$ ,<sup>61,91</sup> and implementing multiple cycles of this process permit extremely controlled thinning process for achieving ultrasharp NWs.<sup>74</sup> The NWs that were thinned down with this process had tapered conical geometry with  $<10\ \text{nm}$  tip diameter.<sup>74</sup> After the thinning process, the ultrasharp Si NW and the surface of the Si substrate were transformed into  $\text{SiO}_2$  NW to prevent electrical cross coupling and leakage currents through the underlying Si substrate. The  $\text{SiO}_2$  NW maintained its ultrasharp tip morphology and retained excellent mechanical stability of its ultrasharp tip which is due to the less porosity and superior mechanical characteristics of thermal oxides compared to that of Plasma Enhanced Chemical Vapor Deposition (PECVD) deposited  $\text{SiO}_2$ .<sup>92,93</sup>

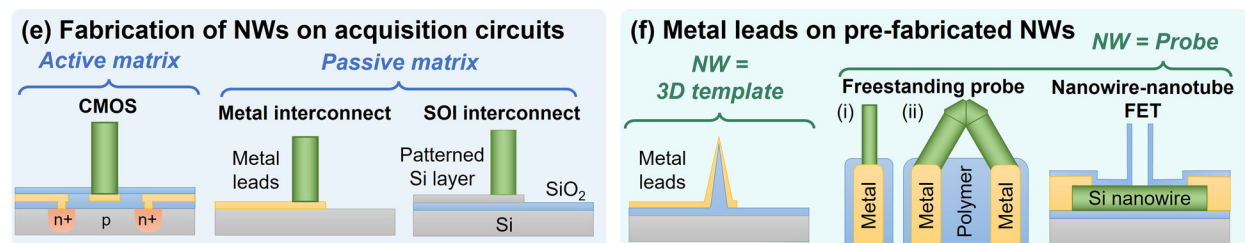
The direct growth of NWs allows the creation of single-crystal NWs on the entire wafer [Fig. 7(b)]. The vapor-liquid-solid (VLS) growth method that uses metal catalyst under chemical vapor deposition system can produce single-crystal NWs with a diameter of 10–100 nm.<sup>94,95</sup> Moreover, the precise tuning of the NW growth conditions allowed the modulation of the growth direction to create kinked-NWs.<sup>96</sup> NWs and nanotubes can also be grown without the use of metal catalysts [Fig. 7(b)].<sup>97,98</sup> For the site-specific growth, the substrate can be masked with amorphous oxide layer with nanoscale hole openings for the selective-area growth of the NWs.<sup>99</sup> Under certain material choice and growth conditions, nanostructures preferentially nucleate and grow along the circular rim of the hole opening, resulting in nanotube structures.<sup>100</sup> Although both VLS and catalyst-free growth methods enable highly controlled growth of nanostructures with superior scalability, the required high process temperature ( $>400^\circ\text{C}$ ) limits the choice of substrates. Hydrothermal growth of NWs is an alternative direct growth strategy that uses solution-based, low-temperature process [Fig. 7(b)].<sup>101</sup> However, the hydrothermal NWs usually require a seed crystal layer for nucleation, and the seed layer prepared with low temperature process is usually polycrystalline.<sup>102</sup> Thus, the hydrothermal NWs grown on top of these seed layers are randomly oriented, which limit the assembly of highly uniform or closely packed intracellular recording probes. Once a seed layer with preferred crystal orientations is prepared under a high temperature,



### ▪ Nanostructure formation



### ▪ Electrical addressing methods of nanostructures



**FIG. 7.** Fabrication approaches for intracellular nanostructures. Processes used to make NWs including (a) top-down etching, (b) direct growth, (c) focused ion beam, and (d) template-assisted methods. The substrate is colored red for the processes that require the substrate to be heated to temperatures above 400 °C. Electrical addressing methods used for intracellular NW/nanotube/nanovolcano recording which include the fabrication of (e) NWs on top of the preexisting acquisition circuits or (f) the definition of metal leads on top of the NWs pre-fabricated on a substrate.

vertically aligned nanostructures can be prepared with the hydrothermal growth process.<sup>102</sup>

Directly writing the NWs under the scanning electron microscope (SEM) equipped with FIB system is another technique to form NWs with narrow diameters on an arbitrary surface [Fig. 7(c)].<sup>47,103</sup> The FIB-assisted deposition created vertical Pt NWs that are 1.5 μm

tall and have a diameter of 150 nm.<sup>47</sup> Alternatively, soft nanotubes can be formed by irradiating the photoresist layer with Ga<sup>+</sup> ion beam, forming solvent-insoluble tubular structure with a typical height and diameter of 1.8 μm and 150 nm, respectively. These can then be coated with Au for both the plasmonic optoporation and electrical recording.<sup>55</sup> However, FIB-assisted methods are serial and

rely on the formation of one nanowire at a time on a small working area of a few millimeters, and the process time tremendously increases with increasing number of channels or samples which limits their scalability.

Template-assisted methods make use of a template with nanoscale 3D features that could later be removed after making the nanostructure [Fig. 7(d)]. The template could be patterned photoresist layers, plastic film with nanopores, or vertical NWs. Electrodeposition of nanostructures through a narrow channel of photoresist layer is a broadly adopted template-assisted approach to make nanostructures on any conducting surface [Fig. 7(d)]. Unlike dry etching, the electrodeposition process does not require the final interface material from the start, but it rather builds amorphous nanostructures through an electrochemical process in a plating solution. By adjusting the electrodeposition time and current, which determines the amount of charge, it is possible to make either cylindrical<sup>104</sup> or dendritic spine-like, mushroom-shaped<sup>53</sup> nanostructures. Although this method is one of the simplest ways to prepare nanostructures on a few samples with limited number of channels, it becomes increasingly challenging as the number of samples or the channel count increases. The duration of the process time surges as both counts increase, and it becomes challenging to maintain a uniform electroplating quality across many channels and samples. To improve the electroplating uniformity on thousands of channels, a closed-loop automatic electrodeposition system was developed where multiple iterations of Pt black electroplating and impedance monitoring can improve the uniformity across the channels.<sup>35</sup> Another issue of electrodeposited nanostructures is in its mechanical stability or structural integrity due to the amorphous nature of the electrodeposited material. This also makes it challenging to create finely controlled structure that was possible with a dry etching approach. One of the smallest diameter NWs prepared by electrodeposition for intracellular recording was 200 nm.<sup>104</sup>

Nanovolcanoes composed of thin nanowalls can be formed by transforming the planar dielectric and metal layers into 3D structures by lithographically patterning the inversely tapered hole in the photoresist template [Fig. 7(d)]. Reactive ion etching process was used to etch and re-sputter the dielectric and metal layers on the substrate to eventually fill the slanted sidewalls of the photoresist patterns.<sup>82,83</sup> This process allows nanometer scale control of nanowall thickness. As such, approximately 100 nm thick nanowalls were prepared, where the metal layer in the nanowall was as thin as 10–20 nm.<sup>82</sup> These ultrasharp nanowall geometry induced high curvature of cell membrane around it, which increased the chance of the nanovolcano to naturally internalize the cell body. This method is advantageous in that it uses a scalable process that can be applied to any substrates or integrated on acquisition circuits. However, because of its micrometer scale diameter (2  $\mu\text{m}$ ), it has limitation in accessing smaller structures of the cell compared to other ultrasharp-tip NW-based approaches.<sup>55,105</sup>

Sharp oxide nanotubes are prepared by coating thin oxide layers on templates with either nanoscale holes within a thin membrane<sup>106</sup> or vertical NWs on a substrate [Fig. 7(d)].<sup>69</sup> Polycarbonate films with nanopores as narrow as 20 nm and as deep as  $\sim 10 \mu\text{m}$  can be formed by passing accelerated high energy heavy ions vertically through the plastic film using a track etching process.<sup>107</sup> An atomic layer

deposition (ALD) system conformally coated a thin oxide layer (10–30 nm) on the entire surface of the template including the inner walls of nanopores. After the oxide deposition, a dry etching process sequentially removed the top oxide layer as well as the upper portion of the polymer film by 1–2  $\mu\text{m}$ , revealing the oxide nanotubes. These oxide nanotubes placed on the nanopores of the membrane are an excellent platform to perform microfluidic interventions with cells<sup>48,108</sup> although electrophysiological recordings were not pursued with this membrane-integrated nanotube platform. Instead of using the nanopore template, vertically grown VLS NWs can be used as a template for growing oxide nanotubes surrounding the NWs. Sharp oxide nanotubes were prepared by conformally coating oxide layers and selectively etching the inner NW.<sup>69</sup> The diameter of the oxide nanotube was controlled down to sub-10-nm by thinning the VLS NW template prior to the ALD  $\text{SiO}_2$  coating.<sup>109</sup>

In addition to the precise formation of NWs, the various electrical addressability strategies are critically important for successful intracellular NW recording. The recording circuit (through the NW with respect to a reference electrode outside the cell body) can be established with (i) the fabrication of NWs on top of the preexisting acquisition circuits [Fig. 7(e)] or (ii) the definition of metal leads on top of the NWs pre-fabricated on a substrate [Fig. 7(f)]. When using the former approach of making NWs on top of the underlying circuit, it is imperative to consider the compatibility of the NW process temperature with the temperature tolerance of the underlying circuits. For example, most of the low temperature NW processes are compatible with CMOS chips or metal leads, but the high temperature NW growth processes ( $>400^\circ\text{C}$ ) and/or thermal oxidation thinning processes ( $\sim 1000^\circ\text{C}$ ) that were discussed above cannot be applied on substrates with pre-patterned metal leads. In a special case when the underlying conducting layers are made with high temperature compatible materials such as patterned passive silicon “device” layers of SOI wafers,<sup>61,110</sup> the high temperature thermal oxidation and thinning process can be performed.

The metal leads to establish recording circuits for NWs prepared under high temperature processes can be deposited on top of the NWs [Fig. 7(f)]. For the vertical NW arrays, the metal layers can be conformally coated on the surface of the NW and etched to define metal traces for electrically addressing the recording NWs.<sup>74,95,101</sup> In this case, the NWs as well as the substrate surface had to be insulating to eliminate any possible currents between the individual metal leads, so the NWs were basically providing 3D nanostructured template to the metal interconnect layer. The VLS-grown NWs are usually transferred onto insulating substrates by solution-based dispersion techniques, and the metal leads can be formed on top of the NWs that lay flat on the substrate surface.<sup>44,45</sup> After the post-assembly, it was also possible to lift off the NW together with the metal leads and polymer support to make kinked<sup>44</sup> or U-shaped<sup>45</sup> NW probes with intracellular recording capability. A single SiC NW<sup>111</sup> or carbon nanotube<sup>112</sup> was also precisely assembled on the tip of quartz micropipettes for intracellular probing. Si NW transistor-based intracellular probes were also fabricated using vertical Ge NWs that were grown by the VLS mechanism from the sidewall of a flat Si NW.<sup>69</sup> This was followed by metal lead formation, oxide layer coating, and finally the removal of the inner Ge NW to result in a vertical oxide nanotube.<sup>69</sup> In such a case, the metal interconnect was formed just after the high temperature VLS growth of the Ge NW.

## VII. NANO-ELECTRODE-CELL INTERFACE FORMATION METHODS AND RECORDING STABILITY

The morphology of the NWs and their internalization mechanism are critical factors to access the intracellular medium.<sup>37,113</sup> Various types of NWs, including NW array,<sup>35,47</sup> gold nanotube,<sup>55</sup> ultrasharp NW,<sup>74</sup> nanovolcano,<sup>82</sup> and U-shaped NW probes,<sup>45</sup> are reviewed in Fig. 6 and their NW-cell interface formation methods are schematically illustrated in Fig. 8(a), alongside an example cross-sectional SEM image of such interface with neurons and ultrasharp NWs in Fig. 8(b). For each approach, the representative recording results of intracellular potentials are presented in Figs. 8(c)–8(j), and the stability of the recording is also discussed. Neuronal recording is more challenging because unlike cardiomyocytes, most neurons do not have regular, periodic firing, and also have interspersed axons that result in different waveform and potential dynamics based on the electrode and cell interface locations.<sup>55</sup> Furthermore, neurons possess relatively softer elastic characteristics and lower stiffness that require more contact forces to penetrate their membranes.<sup>52</sup> Thus, we discuss first the intracellular recordings from CMs [Figs. 8(c)–8(f)] followed by a discussion on neuronal recordings [Figs. 8(g)–8(j)].

Electroporation provides instantaneous intracellular access of NW arrays into the cell body, but the intracellular signal amplitude rapidly decreases with the reconstruction of the cell membrane of HL-1 CMs [Fig. 8(c)].<sup>47</sup> The signal amplitude decayed to 30% 120 s after the electroporation pulse, and the signal returned to extracellular characteristics after 10 minutes. Pt NWs integrated with CMOS electronics also demonstrated typical short-term intracellular coupling responses with amplitude decay for neonatal rat ventricular CMs [Fig. 8(d)].<sup>54</sup> However, for some of the NWs, long-term (~20 min) intracellular coupling without large variance in amplitude was observed [Fig. 8(d)]. The authors attributed the varied intracellular coupling to the variance in electrode-cell interface, wherein some NWs are expelled from recorded cells earlier in time.<sup>54</sup>

In an effort to achieve more stable and sensitive intracellular recording than the electroporation approach, pseudocurrent-clamp (pCC) and pseudovoltage-clamp (pVC) configurations were employed on PtB electrodes integrated atop CMOS electronics that recorded the iPSC-derived neuronal network's intracellular activities.<sup>35</sup> Unlike electroporation that uses brief electrical pulses, pCC configuration injects continuous current (~1 nA) to gradually permeabilize the cell membrane where intracellular coupling (20-fold increase in action potential amplitude) is established after 10 s to a few minutes after the current injection [Fig. 8(d)]. The authors claim that the pCC mode could have advantages over electroporation in that it could be effective in maintaining the cell membrane permeabilization, keeping the membrane potential of the permeabilized neuron near its normal resting potential by compensating leakage current, and allowing concurrent stimulation and recording.<sup>35</sup> However, the intracellular recording under sustained current eventually stopped on its own either by hyperpolarizing neurons (imperfect leakage current compensation) or losing the seal.<sup>35</sup> The duration of intracellular coupling with pCC configuration varied from <10 s to the whole duration of recording (19 min) with median of about 8 min, and the maximum amplitude of the action potentials recorded on individual channels was as large as 10 mV with the median amplitude across channels being 0.2 mV during the neural network burst.<sup>35</sup>

Optoporation is a technique used to concentrate an electromagnetic field at the nanoscale tip of the Au nanostructure which

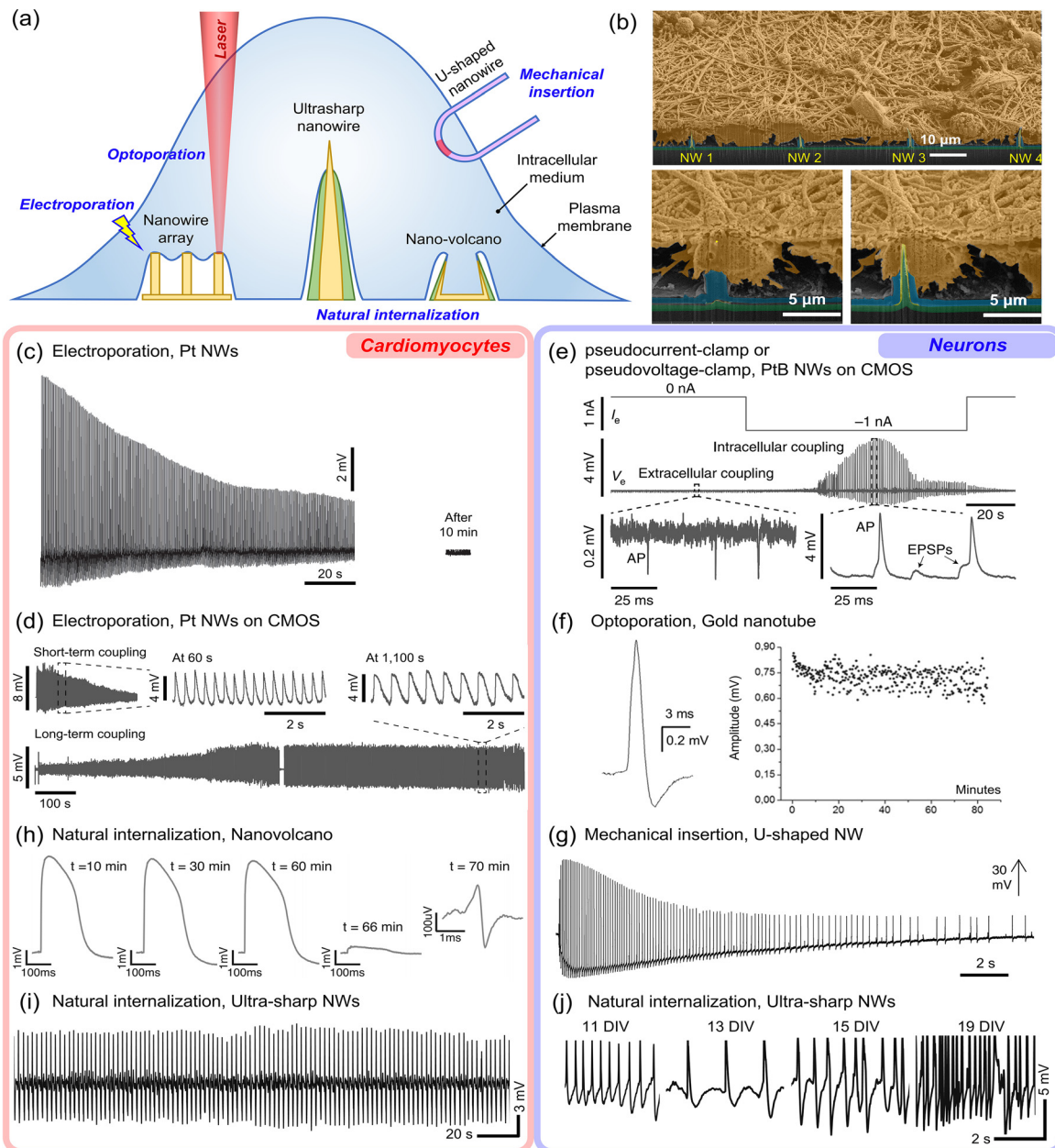
generates nanoshockwaves that can break the cell membrane to allow intracellular access of the nanostructures.<sup>80</sup> With a single-shot optoporation on a rat hippocampal neuron, the potential recorded from the gold nanotube instantly changed from extracellular to intracellular-like potential with its amplitude up to around 2 mV.<sup>55</sup> The intracellular-like potential amplitude was maintained around 0.80–0.95 mV for 80 min [Fig. 8(f)].<sup>55</sup>

Chemical poration is another technique to gain intracellular access by injecting molecules through a nanotube tip to induce a nanopore on the cell membrane by a chemical reaction. Aalipour *et al.* found that both the lipid membrane and actin cytoskeleton act together as synergistic barrier and should be dissociated together for the their nanostraw to access the intracellular medium using molecules that could selectively dissociate the lipid membrane, actin cytoskeleton, or both.<sup>48</sup> Although the chemical poration could be an efficient way for intracellular delivery of molecules, to the best of our knowledge, intracellular potential recordings have not been studied with the chemical poration approach. For the intracellular recording, chemical poration has a few disadvantages compared to electro- and optoporation: (i) While the electro- and optoporation enable instantaneous and highly localized poration,<sup>114</sup> the chemical poration process is expected to take much longer time and impact large population of cells considering the solution exchange process and size of the microfluidic channels.<sup>115</sup> (ii) The prolonged delivery of actin dissociating molecules could cause the cell to lose its integrity (cell blebbing).<sup>48</sup>

Mechanically inserted probes made from ultrafine Si NWs with phospholipid chemical modification showed excellent intracellular recording amplitude upon insertion, but a rapid decrease in the peak amplitude of the action potential amplitude was observed during the first 20 s just after intracellular recording was established with a dorsal root ganglion (DRG) neuron [Fig. 8(g)].<sup>45</sup> The authors suggest that these observed amplitude attenuations are due to either an elastic response from the cytoskeleton or mechanical instability of the measurement setup. On the contrary, precisely engineered ultrafine nanostructures could spontaneously fuse with or internalize into the cell membrane for more stable intracellular recording. Nanovolcano electrodes with 100 nm thin nanowalls naturally fused with the rat CMs and demonstrated stable action potential recording for over one hour without significant change in amplitude [Fig. 8(h)].<sup>82</sup> The nanovolcano initially had thiol-functionalized gold nanoring that could potentially promote the nanovolcano to fuse with the cell membrane. However, it was later found that the geometry of nanovolcano itself was the dominant factor in gaining the intracellular access than the chemical functionalization.<sup>83</sup>

Another approach to facilitate natural internalization of NWs into the cells was to fabricate NWs with precisely engineered ultrasharp tips (USNWs; ultrasharp nanowires) with the tip diameter of 30–70 nm and height of 6–7  $\mu\text{m}$ . On top of these high aspect ratio USNWs, both neuronal (rat primary cortical neurons) and cardiac (induced pluripotent stem cell derived cardiovascular progenitor cells; iPSC-CVPCs) networks were formed. Sequential slicing by a focused ion-beam in the NW arrays revealed strong engulfment of NW by a neuron, which leads to a high probability of spontaneous penetration,<sup>52,90</sup> due to the NW's high aspect ratio and ultrasharp tip [Fig. 8(b)].<sup>74</sup> USNWs recorded CMs consistently firing with no amplitude decay toward extracellular levels (<200  $\mu\text{V}$ ) throughout a total recording time of 372 s [beating interval of 2.05 s; Fig. 8(i)].<sup>74</sup>





**FIG. 8.** Various types of nanostructures and their nanoelectrode-cell interface formation methods. (a) Schematic illustration of multiple NW arrays, U-shaped NW, and nano-volcano and ultrasharp NW tip that forms NW-cell interface by electroporation. Optoporation, mechanical insertion, and natural internalizations, respectively. (b) Cross-sectional SEM images of naturally internalized ultrasharp NWs-neuron interface. Sequential FIB cutting of NW-cell interface revealing NW closely engulfed by a single neuron. Recorded potential from CMs just after the electroporation for (c) Pt nanopillars on quartz and (d) Pt nanoneedles on CMOS. (e) Pseudo-current clamp potential recording of neurons using Pt black (PtB) nanowires on CMOS. (f) Optoporation-enabled spontaneous intracellular-like spike recorded from rat hippocampal neurons using gold nanotube. Amplitude of the positive phase of action potentials after the optoporation. (g) Potential recording of neurons upon the mechanical insertion of U-shaped NW. (h) Rat CMs potential recorded with the naturally internalized nanovolcano electrode. (i) Intracellular recordings of cardiac activity from USNWs with consistent spiked action potentials without amplitude decay during the 6 min recording time. (j) Consistently large intracellular-like action potentials recorded from rat cortical neurons using USNWs across 11–19 days *in vitro* (DIV). Edited and reprinted with permission from Liu *et al.*, *Adv. Func. Mat.* 2108378 (2021). Copyright 2021 IEBL.<sup>74</sup> Edited and reprinted with permission from Xie *et al.*, *Nat. Nanotechnol.* 7, 185 (2012). Copyright 2012 Macmillan Publishers.<sup>47</sup> Edited and reprinted with permission from Abbott *et al.*, *Nat. Nanotechnol.* 12, 460 (2017). Copyright 2017 Macmillan Publishers.<sup>54</sup> Edited and reprinted with permission from Dipalo *et al.*, *Nano Lett.* 17, 3932 (2017). Copyright 2017 American Chemical Society.<sup>55</sup> Edited and reprinted with permission from Zhao *et al.*, *Nat. Nanotechnol.* 14, 783 (2019). Copyright 2019 Macmillan Publishers.<sup>45</sup> Reprinted with permission from Desbiolles *et al.*, *Nano Lett.* 19, 6173 (2019). Copyright 2019 American Chemical Society.<sup>32</sup> Edited and reprinted with permission from Abbott *et al.*, *Nat. Biomed. Eng.* 4, 232 (2020). Copyright 2020 Macmillan Publishers.<sup>35</sup>



Additionally, the USNWs showed a stable NW-neuron interface to record intracellular potentials for a continuous 5–6 min and across 11–19 DIV [Fig. 8(j)].<sup>74</sup> The natural intracellular penetration of the neuron's cellular membrane permitted large amplitude of recorded action potentials in the spike trains that did not diminish to extracellular levels. These spike trains manifested intracellular features with excitatory postsynaptic potential (EPSP) events. This amplitude was clipped in many instances to the maximum range of the Intan recording amplifiers of  $\sim 10$  mV. These are the first electrophysiological results demonstrating reliable NW recordings of neuronal action potential trains with clear graded potentials and without any additional electroporating manipulation, elevating the promise of this technology for longitudinal and reliable intracellular electrophysiology from networks of neurons and brain organoids.

Many different approaches are utilized for fabricating vertical nanoelectrodes for intracellular electrophysiology as discussed above. Generally, when designing NW arrays for spontaneous intracellular electrophysiology purposes without any additional electroporation or optoporation methods, it is imperative to be mindful of various design parameters that can enable intracellular capabilities and that can also provide a secure platform for cultured cell viability. The NW geometry, substrate material, and additional surface treatments have all shown to influence the intracellular capabilities and the cell culture health.

### A. Effect of Nanowire geometry for intracellular capabilities

To a great extent, the density and the diameter of NWs are critical factors in determining the nature of interaction between the NW and the cells, including the degree of cell membrane bending around the NWs and the force required between the cell and NW for spontaneous cell membrane penetration.<sup>37,116</sup> Generally, passive penetration of the high aspect ratio NWs into the cell by inducing rupturing of cell membrane's lipid bilayer depends on a number of factors such as gravitational forces, cellular hydrostatic pressure, and the free energy of cell membrane from surface tension as well as the elastic energy from membrane deformation. Various models have been developed and analyzed to study this spontaneous intracellular penetration. Investigations by Xie *et al.* suggested that penetration is influenced by the adhesion between the main substrate and the cell, the geometry and arrangement of the nanostructure and its array, and the specific cell line's stiffness. Primarily, adhesion between the main substrate and the cell has been considered to be important since it has been modeled that relying purely on gravitational force would require NW tip diameters  $< 10$  nm for unassisted cell penetration.<sup>52</sup> With regard to the NW geometry, the required penetration force decreases linearly with decreasing the NW radii; with critical penetration tension of 5.6 mN/m, penetration would be unlikely for a NW with a radius greater than 150 nm. Moreover, as the NW height increases, its contact angle with the cell membrane increases, and as a result, less penetration force is required. NW arrays with a reduced inter-NW spacing and higher NW areal density, can impair cell's contact with the substrate and limit the penetration force and the probability of penetration especially for stiffer cells.<sup>52</sup> Lou *et al.* emphasized the importance of the nanostructures' small diameter ( $< 500$  nm), intermediate density based on the cell line being tested, and the applicable height in influencing appropriate deformation of the cell plasma membrane, which were consistent with the findings of Xie *et al.*<sup>117</sup> Also, Xie *et al.*

more recently observed that the time window at which the NW can penetrate the cell is limited since the effective adhesive force reduces over time with the reduction of contact area between cell and the substrate surface.<sup>90</sup> Alternatively, Buch-Månson *et al.* and Zhou *et al.* have also modeled the vertical nanostructure penetration by focusing instead on the changes in membrane free energy.<sup>118,119</sup> In agreement with the previous modeling results, Buch-Månson *et al.* and Zhou *et al.* stressed that sharper NWs induce greater probability of membrane deformation for penetration.<sup>118,119</sup> Capozza *et al.* have also showed the role of the membrane lipid bilayer bending, curvatures, and traction forces in intracellular penetration with vertical pillars and specifically noted the role of pillar's edge sharpness.<sup>120</sup> With ample sharpness at the edge, hence a low radius of curvature of around  $20 \pm 5$  nm, there is a considerable decrease in tensile strength necessary for membrane rupture, which explains both membrane penetration observed with sharp, high aspect ratio nanoelectrodes, and providing evidence that permeabilization might be possible even for vertical structures with  $> 2$   $\mu$ m diameter, provided there is considerable edge sharpness. Overall, to increase the likelihood of spontaneous penetration, the choice of and control over the NWs' radius, height, and spacing is imperative; thin, sparse NW array is a desired design criterion that ultimately promotes successful cell membrane penetration.

### B. Cell culture viability modulation via substrate material and preparation

Additionally, to have a successful recording of the intracellular activities *in vitro* with the nanostructured platform, culturing robust cells are as important as designing optimal nanostructures with appropriate geometry. Considering that the NWs typically occupy a small area on the substrate, the majority of the cell membrane actually interfaces with the surface of the top-most passivation layers of the NW platform. There has also been extensive studies on the effect of substrate topography, roughness, and elasticity on the viability of the cell culture.<sup>121,122</sup> As discussed previously, the adhesion between the cell and the substrate plays an integral role in increasing likelihood of penetration for well-defined vertical nanostructures with appropriate geometry for particular cell line; this surface adhesion has been greatly influenced through substrate material properties and treatments. Beyond surface adhesion, cellular responses such as cellular morphology, degree of proliferation, differentiation, and cell death are all influenced by substrate topography, roughness, and elasticity.<sup>121</sup>

As introduced previously, vertical topography and electrode array arrangement affect the degree of intracellular penetration capability. All the more, vertical topography changes with vertical pillars with varying sizes and spacings have also shown to increase cell migration and motility (the spontaneous movement of a cell from one location to another related to overall cell health) through modulation of cell to substrate interactions and augmentation of the size and lifetime of the focal contacts at the edges of the vertical structures.<sup>123</sup> Vertical nanopillars were also shown to enhance surface protein adsorption, which dictates cell-to-cell interactions, cellular signaling events, and cellular response to the substrate surface, possibly due to spatial changes in the orientation and density of the adsorbed protein with the substrates.<sup>124</sup> While surface topography modulation via vertical structures might still compose a limited portion of the entire culture area, evidences<sup>105,122</sup> suggest that it is likely that they still would increase the cellular viability near the recording sites.

Moreover, the substrate surface roughness has shown substantial impact on the adhesion of cultured cells. Polymeric surface roughening performed via slurry polishing (four- to ninefold roughness increases compared to native surface, root mean square (RMS) surface roughness of 7–18 nm) on polymers such as SU-8, 1002F, and polydimethylsiloxane (PDMS) increased cellular adhesion and capture efficiency from three- to ninefold for all cell lines tested [HeLa, 3T3, and Rat Basophilic Leukemia (RBL) cells].<sup>125</sup> Furthermore, parylene C, another biocompatible polymeric material, has illustrated excellent mammalian cell adhesion properties (tested on NIH-3T3 fibroblasts and AML-12 hepatocytes) after proper surface roughening via O<sub>2</sub> plasma treatment.<sup>126</sup> This excellent adhesion was attributed to the inherent nanoscale surface roughness of biocompatible parylene C and its stable hydrophilic surface for cell adherence after plasma treatment. For example, the surface of USNW devices was passivated with a dual layer of SiO<sub>2</sub> and parylene C, which was then exposed to a brief O<sub>2</sub> plasma treatment to generate an RMS surface roughness of 7 nm to improve neuronal and cardiac adhesion and network formation of rat primary cortical neurons and iPSC-CVPCs. The surface roughness of the overall platform as well as the neuronal culture area<sup>76</sup> was found to play a critical role in promoting neuronal adhesion and network formation in multi-layered 3D neuronal structures.<sup>74</sup>

Finally, the substrate elasticity have also been observed to govern cellular processes, responses, and viability due to the intrinsic, physical deformations present *in vivo* extracellular environments of tissues themselves.<sup>121</sup> Various surface treatments and substrate materials are utilized to mimic and tune extracellular elasticity, which include numerous materials with varying elastic moduli, such as synthetic and natural polymers from PDMS, polymethyl methacrylate (PMMA), polyethylene glycol (PEG), and hydrogels such as agarose and Matrigel. Various extracellular matrix proteins are also applied for enhanced cell adhesions such as fibronectin, laminin, RGD peptides, collagen, and poly-L-lysine.<sup>74,121</sup>

Chemical modifications can also provide intracellular access, particularly with vertical nanoelectrodes that employ gentle, mechanical contact/insertion techniques. Such devices include kinked NWs,<sup>44,96</sup> branched nanotube FETs,<sup>69</sup> and U-shaped NW FETs,<sup>45</sup> where the interface electrodes have been chemically modified with phospholipid coatings that mimic the lipid bi-layer of the cell membrane to induce spontaneous intracellular penetration via merging of the membrane and the modified electrode.<sup>44,45,69</sup>

Therefore, the surface material of the substrate and any modifications via roughening treatments enhances the viability cultured cells and further chemical applications can improve cell adhesion and even facilitate spontaneous intracellular penetration for certain nanoelectrodes.

### VIII. EXPERIMENTAL VALIDATION OF THE CRITICAL IMPORTANCE OF SINGLE VS MULTIPLE NANOWIRES PER ELECTRODE

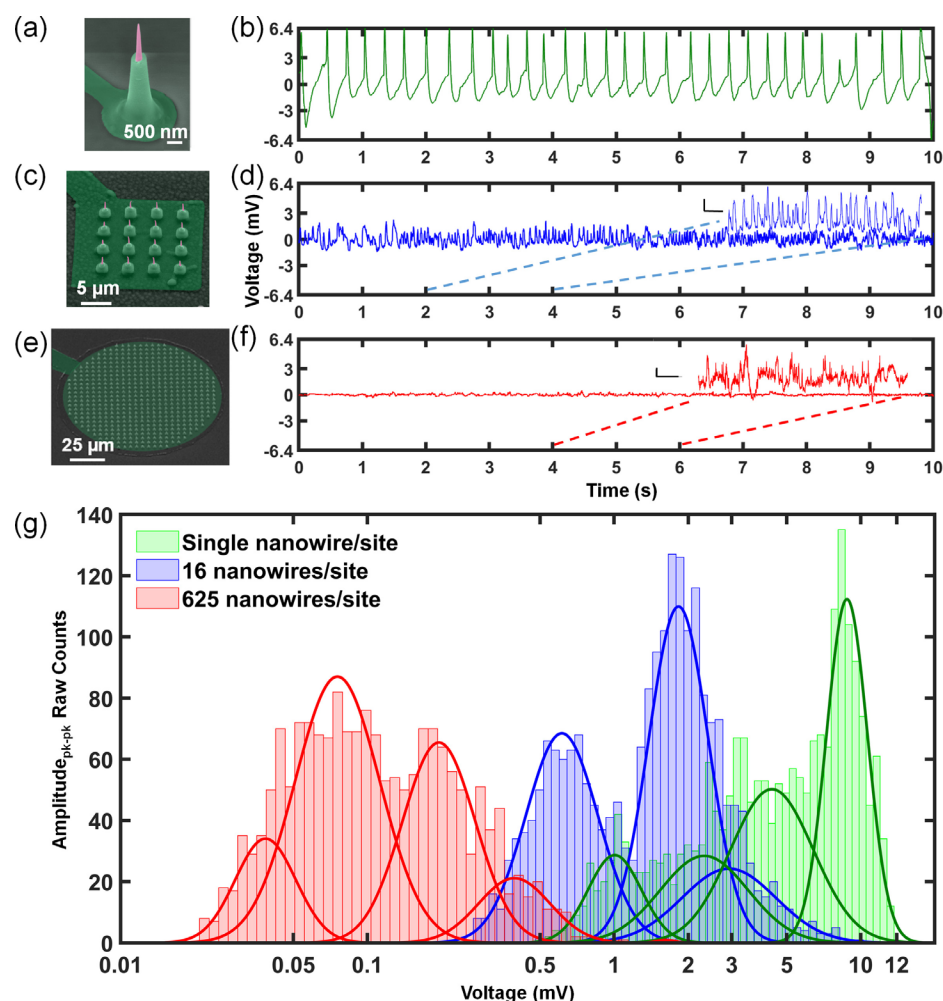
Section IV and Fig. 4 indicated the critical role of single Nanowires per electrode for recording of intracellular potentials with large coupling coefficients or high sensitivity. Further experiments that utilized three different types of ultrasharp vertical NW arrays that have a single NW [Figs. 9(a) and 9(b)], 16 NWs [Figs. 9(c) and 9(d)], or 625 NWs [Figs. 9(e) and 9(f)] per channel have further corroborated these results. Electrophysiological recordings commenced on 7 DIV from cultured rat primary cortical neurons. While both platforms

showed clear spike trains, the peak-to-peak amplitude histogram of the recorded action potentials [Fig. 9(g)] shows that the most frequently observed amplitude of single NWs was as large as ~9 mV and that from 16 and 625, NWs were ~2 mV and ~60  $\mu$ V, respectively, which are 4 and 1500 times smaller, even without accounting for potential clipping due to the amplifier range of  $\pm 6.4$  mV.<sup>74</sup> The recorded spike train of action potentials from individually addressable NWs shows intracellular features indicative of EPSPs, whereas the spike train recorded from multiple NWs did not show these features. These experimental results, validated with cross-sectional microscopy, pharmacology, and electrical interventions,<sup>74</sup> are in good agreement with the modeling results of Fig. 4 that predicted exponential decay for the amplitude of recorded spikes with the number of extracellular NWs per single channel, explaining the reason for smaller amplitudes recorded by preceding NW technologies.

### IX. VALIDATING THE ELECTROPHYSIOLOGICAL ORIGIN OF POTENTIALS RECORDED BY NANOWIRE INTERFACES

It is crucial to validate whether the potential being measured with any new electrode technologies is electrophysiological. Various methods used to validate intracellular access of the NW into the cell are schematically illustrated in Fig. 10(a). One of the best ways to directly validate this is to measure a single cell simultaneously with the “gold standard” patch clamp and the nanostructured electrode. This concurrent measurement was done for gM $\mu$ E where a large non-mammalian Aplysia neuron was cultured on top of the electrode array, and the same cell was measured with sharp glass micropipette.<sup>53,75</sup> After forming the intracellular interface by electroporation, the calibrated potentials that were recorded from both the gM $\mu$ E and the sharp electrode were nearly identical to each other including the sub-threshold potentials [Fig. 10(b)]. Kinked NW probe also simultaneously recorded the same targeted CM with whole-cell patch clamp pipette [Fig. 10(c)].<sup>44</sup> Upon entry into the cell (triangle), raw signals recorded from kinked NW probe (blue) and the patch clamp (red) showed nearly similar waveforms.

Another way to characterize the entry of NW probe into the intracellular medium is to measure the resting potential of the cell. The kinked NW probe coated with phospholipid bilayers showed a sharp drop of ~52 mV within 250 ms after cell-to-tip contact [Fig. 10(d)].<sup>96</sup> Constant ~-46 mV was maintained, while the nanoprobe was inside the cell, and the potential went back to baseline as the nanoprobe was detached from the cell. Pharmacological intervention is another effective method to validate the electrophysiological origin of potentials recorded by NWs as it can modulate the shape, amplitude, and frequency of neuronal activity. There are many pharmacological interventions in the function of the ion channels on the neuronal membranes. Pharmacological validation can be advantageous over patch clamp when the NW electrode measures a cell deep inside the tissue that is inaccessible to patch pipettes. The intracellular current measured by the Pt-black/Pt nanoneedles<sup>35</sup> was modulated using ion channel-targeting tetrodotoxin (TTX, Na<sup>+</sup> channel blocker) and tetraethylammonium (TEA, K<sup>+</sup> channel blocker) [Fig. 10(e)] which confirmed the electrophysiological origin of the measured currents. For the ultrasharp NWs, the addition of picrotoxin (PTX;  $\gamma$ -Aminobutyric acid type A receptor GABA<sub>A</sub> receptor antagonist) gradually increased the frequency and the amplitude of action



**FIG. 9.** Single vs multiple NWs per electrode. SEM images and recorded spike train of action potentials of (a) and (b) single NW, (c) and (d) 16, (e) and (f) 625 multiple NWs per pad electrode arrays. (g) Histogram of peak-to-peak signal amplitude between single USNW and multi-USNWs per site. Vertical scale bars in (d) and (f) are  $500\ \mu\text{V}$  and  $200\ \mu\text{V}$ , respectively, and their lateral scale bar is 250 ms. Reprinted with permission from Liu *et al.*, *Adv. Func. Mat.* 2108378 (2021). Copyright 2021 IEBL.<sup>74</sup>

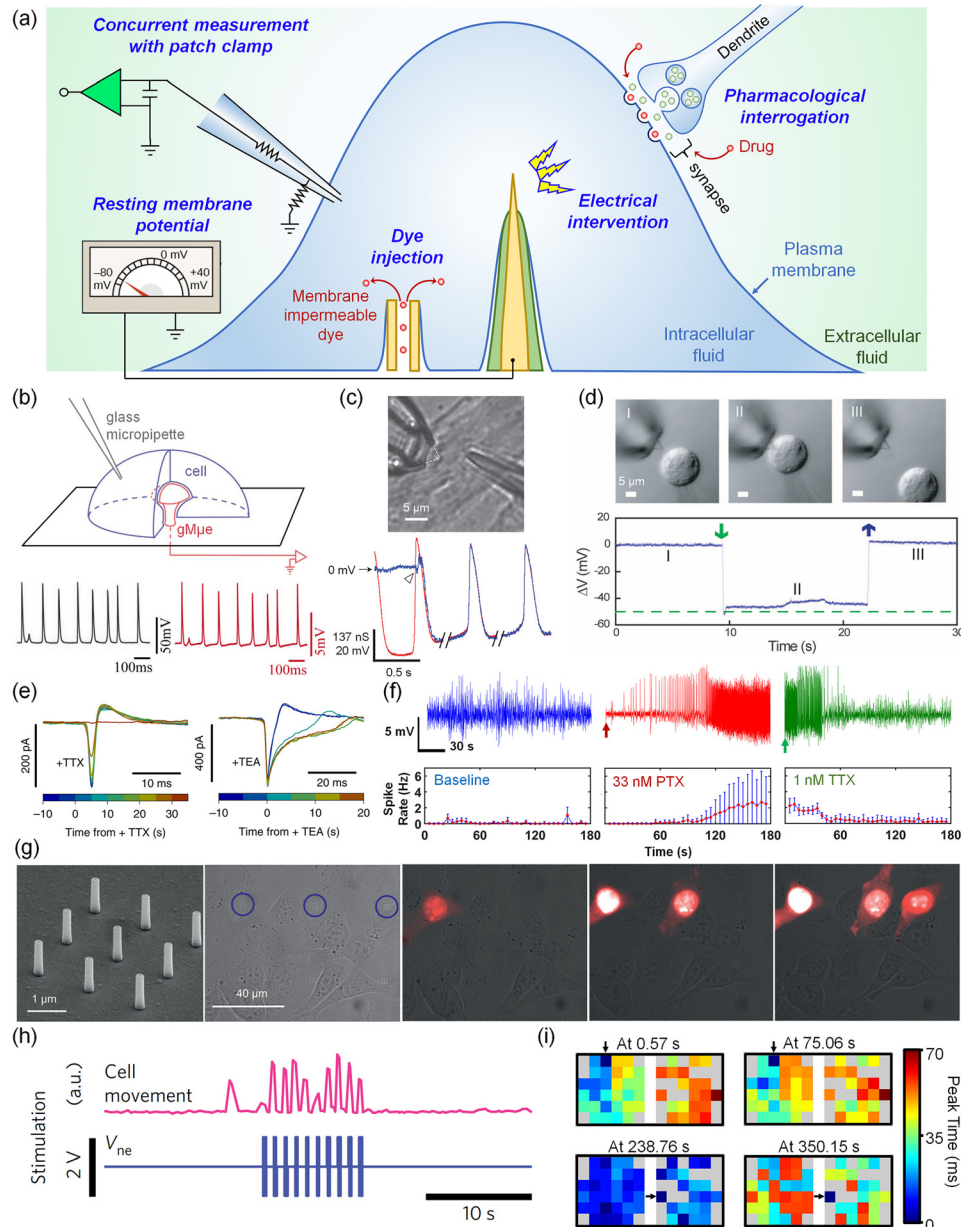
potentials, whereas TTX suppressed firing [Fig. 10(f)].<sup>74</sup> The lag in electrophysiological changes after both PTX and TTX application are believed to be related to the inherent delay for the compounds to diffuse through the multiple layers of neurons before accessing the bottom-most layer that the NW recorded.

For vertical nanotube devices, a direct validation of the nanotube penetration through the plasma membrane of the cell can be accomplished with the injection of a membrane impermeable dye into the cell body through the nanotube [Fig. 10(a)]. Upon irradiating a pulsed laser on the gold nanotubes to open the channel between the nanotube tip and the cell by the optoporation process, propidium iodide (PrId), a membrane impermeable dye that binds to DNA, was passed into the cell through the nanotube.<sup>80</sup> Once the dye entered the intracellular medium, the cell displayed a fluorescence signal. The sequential optoporation of the gold nanotube arrays interfacing with cell followed by fluorescence signal from each cell indicates the intracellular access of the nanotubes [Fig. 10(g)]. Additionally, the transient characteristics of nanopores formed by the optoporation process were investigated by delaying the PrId delivery after the laser irradiation. It was found that the lifetime of the nanopore on the membrane formed by

optoporation was nearly 10 min with a small variation between the cells.<sup>80</sup> Electroporation-enabled intracellular access of nanotubes was also validated by delivering both non-permeant (PrId) and permeant (calcein-AM) molecules into the cell membrane that expressed different fluorescent colors.<sup>127</sup>

Once a reliable electrochemical interface between the cell and the NW is formed, it also becomes possible to electrically stimulate the cells to modulate activity. The NW-based electrical stimulation study of single neuron showed that intracellular stimulation provides superior characteristics in activating  $\text{Ca}^{2+}$  responses and a faster recovery rate compared to extracellular stimulation.<sup>128</sup> Pt nanoneedles stimulated biphasic voltage pulse sequences on CMs to induce action potentials [Fig. 10(h)], and it was possible to modulate the beating frequency of CMs from 0.05 to 1 Hz.<sup>54</sup> USNWs used active electrical stimulation and mapping capabilities to illustrate spatial modulation of the action potential propagation direction within cardiac tissues [Fig. 10(i)].<sup>74</sup> Two intracellular recordings before electrical stimulation show action potential propagation from left to right [upper panels in Fig. 10(i)], whereas intracellular recordings after electrical stimulation show an evolution from homogeneous propagation [lower left panel in Fig. 10(i)] to reversed





**FIG. 10.** NW-cell electrochemical interface validation methods. (a) Schematics of the methods used to validate intracellular access of the NW into the cell. (b) Intracellular potential measured with sharp glass electrode (black) and gMμE (red). (c) Differential interference contrast image and recorded potential from kinked NW transistor probes (left; blue) and whole-cell patch clamp (right; red) recording the same cell. (d) Kinked NW transistor probes measuring the resting membrane potential upon internalization into the cell membrane. Pharmacological modulation of action potentials for (e) Pt-black-Pt nanoneedles and (f) ultrasharp Pt NWs. (g) Sequential optoporation of gold nanotubes-cell interfaces that enabled the membrane impermeable dye to be injected into the cell bodies through the nanotubes' microfluidic channel. (h) Electrical bi-phasic stimulation of CMs through the Pt nanoneedles that evoked synchronized cell movement. Movement was analyzed from optical microscope video differentials. (i) Electrical stimulation of CM networks with selected ultrasharp NWs altering the propagating pattern of action potentials. The original pacemaker foci locations are labeled with arrows. Edited and reprinted with permission from Avissar *et al.*, *Biology* (OpenStax, 2013). Copyright 2013 OpenStax. Edited and reprinted with permission from Hai *et al.*, *Lab Chip* **12**, 2865 (2012). Copyright 2021 Royal Society of Chemistry.<sup>53</sup> Edited and reprinted with permission from Shmuel *et al.*, *Sci. Rep.* **6**(1), 27110 (2016). Copyright 2016 Macmillan Publishers.<sup>76</sup> Edited and reprinted with permission from Qing *et al.*, *Nat. Nanotechnol.* **9**, 142 (2014). Copyright 2014 Macmillan Publishers.<sup>44</sup> Edited and reprinted with permission from Tian *et al.*, *Science* **329**, 830 (2010). Copyright 2010 AAAS.<sup>96</sup> Edited and reprinted with permission from Abbott *et al.*, *Nat. Biomed. Eng.* **4**, 232 (2020). Copyright 2020 Macmillan Publishers.<sup>39</sup> Edited and reprinted with permission from Messina *et al.*, *Adv. Mater.* **27**(44), 7145 (2015). Copyright 2015 Wiley-VCH.<sup>50</sup> Reprinted with permission from Abbott *et al.*, *Nat. Nanotechnol.* **12**, 460 (2017). Copyright 2017 Macmillan Publishers.<sup>54</sup> Reprinted with permission from Liu *et al.*, *Adv. Func. Mat.* 2108378 (2021). Copyright 2021 IEBL.<sup>74</sup>



direction that originates from right to left [lower right panel in Fig. 10(i)], where the action potential propagation starts from the stimulating electrode. The results presented here show high spatiotemporal resolution electrophysiological mapping and simultaneous interrogation in cardiac tissues for control of cardiac activity.

## X. CONCLUSION AND OUTLOOK

This paper discussed foundations in NW electrophysiological recordings of neurons that can also be applicable to interrogations to other types of excitatory cells. Electrochemical aspects of the interface and material choice play an important role in the sensitivity of NWs to neuronal activity. The significance of proper circuit analysis of the NW-neuron interfaces was illustrated by discussing multiple interface configurations and the gained insights supported our experimental results, which highlight the critical need for individual electrical addressability in these interfaces. We surveyed progress in this domain and presented recent results from our laboratory on the natural intracellular recordings of large amplitude action potential spikes with the ability to record subthreshold oscillations.

Despite the meaningful progress surveyed here, there are two significant challenges to be overcome in NW-neuron interfaces. The first is embodied in the temporal resolution of NWs, whose large impedance together with the large parasitic capacitance lead to large RC time constants that spread the recorded action potentials. These can be minimized by introducing capacitive cancellation techniques on the amplifier end or the direct integration of NWs on amplifiers without long metal leads that give rise to the parasitic capacitance. The other is embodied in the selective interrogation of networks and mapping how subthreshold oscillations modulate network activity. These can be supported by longitudinal recordings in environments supporting viability of the culture and compatibility with the recording electronic interfaces. The two major consequences of such near-term advances include first the ability to interrogate at high spatiotemporal electrophysiological resolution of functional synthetic organoids for basic neuroscience and drug screening. The second major consequence is the natural merging of *in silico* and *in vitro* neuronal networks that can truly merge artificial intelligence with natural biological intelligence and function.

## ACKNOWLEDGMENTS

This work was performed with the gracious support of National Science Foundation under Award Nos. ECCS-1351980 (CAREER) and CMMI-1728497 for S.A.D. and DGE-1650112 for A.M.B. and of the National Institutes of Health under Award Nos. NBIB DP2-EB029757 and NINDS R01-NS123655-01 and NINDS UG3-NS123723-01 for S.A.D. S.A.D. and R.L. also acknowledge the gracious support of the UC-National Laboratory in Residence Graduate Fellowships (UC-NLGF), Award No. 477131. This work was performed, in part, at the Center for Integrated Nanotechnologies, an Office of Science User Facility operated for the U.S. Department of Energy (DOE) Office of Science. Los Alamos National Laboratory, an affirmative action equal opportunity employer, is managed by Triad National Security, LLC for the U.S. Department of Energy's NNSA (Contract No. 89233218CNA000001) and Sandia National Laboratories (Contract No. DE-AC04-94AL85000) through a CINT user proposal. This work was performed in part at the San Diego Nanotechnology Infrastructure (SDNI) of UCSD, a member of the National

Nanotechnology Coordinated Infrastructure, which is supported by the National Science Foundation (Grant No. ECCS-1542148). The authors thank technical support from the Integration Laboratory at CINT and from the nano3 clean room facilities at UC San Diego's Qualcomm Institute. The authors acknowledge Po Chun Chen for assistance in doping and characterizing the SOI device layer used for the Si electrodes tested here. The authors acknowledge technical discussions with Dr. Renjie Chen, Dr. Atsunori Tanaka, and Dr. Massoud L. Khraiche, and the contributions of Dr. Deborah Pre, Dr. Agnieszka D'Antonio-Chronowska, Dr. Gaelle Robin, Dr. Kelly A. Frazer, and Dr. Anne G. Bang for cellular culture. The authors also acknowledge discussions and technical support from Dr. John Nogan, Dr. Jennifer Martinez, Dr. Katherine L. Jungjohann, Anthony R. James, Douglas V. Pete, and Denise B. Webb of Sandia National Laboratories.

## AUTHOR DECLARATIONS

### Conflict of Interest

The authors have no conflicts to disclose.

## DATA AVAILABILITY

The data that support the findings of this study are available from the corresponding author upon reasonable request.

## REFERENCES

- <sup>1</sup>R. Williams, *Annu. Rev. Neurosci.* **11**, 423 (1988).
- <sup>2</sup>S. Herculano-Houzel, *Front. Hum. Neurosci.* **3**, 31 (2009).
- <sup>3</sup>R. S. J. Frackowiak, *Human Brain Function* (Elsevier, 2004).
- <sup>4</sup>R. L. Buckner, J. Sepulcre, T. Talukdar, F. M. Krienen, H. Liu, T. Hedden, J. R. Andrews-Hanna, R. A. Sperling, and K. A. Johnson, *J. Neurosci.* **29**, 1860 (2009).
- <sup>5</sup>J. D. Power, A. L. Cohen, S. M. Nelson, G. S. Wig, K. A. Barnes, J. A. Church, A. C. Vogel, T. O. Laumann, F. M. Miezin, B. L. Schlaggar, and S. E. Petersen, *Neuron* **72**, 665 (2011).
- <sup>6</sup>V. B. Mountcastle, *J. Neurophysiol.* **20**, 408 (1957).
- <sup>7</sup>J. G. Horton and D. L. Adams, *Philos. Trans. R. Soc. B Biol. Sci.* **360**, 837 (2005).
- <sup>8</sup>J. J. Gargus, *Ann. N. Y. Acad. Sci.* **1151**, 133 (2009).
- <sup>9</sup>D. M. Kullmann, *Brain* **125**, 1177 (2002).
- <sup>10</sup>P. Imbrici, M. C. D'Adamo, A. Grottesi, A. Biscarini, and M. Pessia, *Am. J. Physiol.—Cell Physiol.* **300**, 1314 (2011).
- <sup>11</sup>P. Fattahi, G. Yang, G. Kim, and M. R. Abidian, *Adv. Mater.* **26**, 1846 (2014).
- <sup>12</sup>N. J. Willumsen, M. Bech, S. P. Olesen, B. S. Jensen, M. P. G. Korsgaard, and P. Christophersen, *Recept. Channels* **9**, 3 (2003).
- <sup>13</sup>B. Biswal, F. Zerrin Yetkin, V. M. Haughton, and J. S. Hyde, *Magn. Reson. Med.* **34**, 537 (1995).
- <sup>14</sup>F. Zhang, V. Gradinaru, A. R. Adamantidis, R. Durand, R. D. Airan, L. D. Lecea, and K. Deisseroth, *Nat. Protoc.* **5**, 439 (2010).
- <sup>15</sup>M. E. Shenton, H. M. Hamoda, J. S. Schneiderman, S. Bouix, O. Pasternak, Y. Rath, M. A. Vu, M. P. Purohit, K. Helmer, I. Koerte, A. P. Lin, C. F. Westin, R. Kikinis, M. Kubicki, R. A. Stern, and R. Zafonte, *Brain Imaging Behav.* **6**, 137 (2012).
- <sup>16</sup>C. Grienberger and A. Konnerth, *Neuron* **73**, 862 (2012).
- <sup>17</sup>R. Y. Tsien, *Ann. Rev. Biophys. Bioeng.* **12**, 91 (1983).
- <sup>18</sup>H. A. Clark, M. Hoyer, M. A. Philbert, and R. Kopelman, *Anal. Chem.* **71**, 4831 (1999).
- <sup>19</sup>M. E. Spira and A. Hai, *Nat. Nanotechnol.* **8**, 83 (2013).
- <sup>20</sup>D. R. Kipke, W. Shain, G. Buzsáki, E. Fetz, J. M. Henderson, J. F. Hetke, and G. Schalk, *J. Neurosci.* **28**, 11830 (2008).
- <sup>21</sup>G. Buzsáki, *Nat. Neurosci.* **7**, 446 (2004).
- <sup>22</sup>M. F. Bear, B. W. Connors, and M. A. Paradiso, *Neuroscience* (Lippincott Williams & Wilkins, 2007).

- <sup>23</sup>A. L. Hodgkin and B. Katz, *J. Physiol.* **108**, 37 (1949).
- <sup>24</sup>D. R. Merrill, *Implantable Neural Prostheses* (Springer, 2010), Vol. 2, pp. 85–138.
- <sup>25</sup>O. P. Hamill, A. Marty, E. Neher, B. Sakmann, and F. J. Sigworth, *Pflügers Arch.* **391**, 85 (1981).
- <sup>26</sup>A. Molleman, *Patch Clamping: An Introductory Guide to Patch Clamp Electrophysiology* (John Wiley & Sons, 2003).
- <sup>27</sup>T. Akita, M. Ohara, and Y. Okada, “Patch-clamp techniques: General remarks,” in *Patch Clamp Techniques* (Springer, 2012), pp. 21–41.
- <sup>28</sup>E. Neher, B. Sakmann, and J. H. Steinbach, *Pflügers Arch. Eur. J. Physiol.* **375**, 219 (1978).
- <sup>29</sup>E. Neher and B. Sakmann, *Nature* **260**, 799 (1976).
- <sup>30</sup>D. Lipscombe and C. P. Toro, *Biophysics of Voltage-Gated Ion Channels* (Academic Press, 2014).
- <sup>31</sup>R. T. Mathias, I. S. Cohen, and C. Oliva, *Biophys. J.* **58**, 759 (1990).
- <sup>32</sup>C. Mathes, *Expert Opin. Ther. Targets* **10**, 319 (2006).
- <sup>33</sup>S. B. Kodandaramaiah, G. T. Franzesi, B. Y. Chow, E. S. Boyden, and C. R. Forest, *Nat. Methods* **9**, 585 (2012).
- <sup>34</sup>P. B. Kruskal, Z. Jiang, T. Gao, and C. M. Lieber, *Neuron* **86**, 21 (2015).
- <sup>35</sup>J. Abbott, T. Ye, K. Krenke, R. S. Gertner, S. Ban, Y. Kim, L. Qin, W. Wu, H. Park, and D. Ham, *Nat. Biomed. Eng.* **4**, 232 (2020).
- <sup>36</sup>A. F. McGuire, F. Santoro, and B. Cui, *Annu. Rev. Anal. Chem.* **11**, 101 (2018).
- <sup>37</sup>S. G. Higgins, M. Becce, A. Belessiotis-Richards, H. Seong, J. E. Sero, and M. M. Stevens, *Adv. Mater.* **32**, 1903862 (2020).
- <sup>38</sup>W. Kim, J. K. Ng, M. E. Kunitake, B. R. Conklin, and P. Yang, *J. Am. Chem. Soc.* **129**, 7228 (2007).
- <sup>39</sup>A. Hai, A. Dormann, J. Shappir, S. Yitzchaik, C. Bartic, G. Borghs, J. P. M. Langedijk, and M. E. Spira, *J. R. Soc. Interface* **6**, 1153 (2009).
- <sup>40</sup>J. Miao, W. Hu, N. Guo, Z. Lu, X. Liu, L. Liao, P. Chen, T. Jiang, S. Wu, J. C. Ho, L. Wang, X. Chen, and W. Lu, *Small* **11**, 936 (2015).
- <sup>41</sup>B. Tian and C. M. Lieber, *Chem. Rev.* **119**, 9136 (2019).
- <sup>42</sup>D. Xu, J. Mo, X. Xie, and N. Hu, *Nano-Micro Lett.* **13**, 1 (2021).
- <sup>43</sup>J. Abbott, T. Ye, D. Ham, and H. Park, *Acc. Chem. Res.* **51**, 600 (2018).
- <sup>44</sup>Q. Qing, Z. Jiang, L. Xu, R. Gao, L. Mai, and C. M. Lieber, *Nat. Nanotechnol.* **9**, 142 (2014).
- <sup>45</sup>Y. Zhao, S. S. You, A. Zhang, J. H. Lee, J. Huang, and C. M. Lieber, *Nat. Nanotechnol.* **14**, 783 (2019).
- <sup>46</sup>R. Liu, R. Chen, A. T. Elthakeb, S. H. Lee, S. Hinckley, M. L. Khraiche, J. Scott, D. Pre, Y. Hwang, A. Tanaka, Y. G. Ro, A. K. Matsushita, X. Dai, C. Soci, S. Biesmans, A. James, J. Nogan, K. L. Jungjohann, D. V. Pete, D. B. Webb, Y. Zou, A. G. Bang, and S. A. Dayeh, *Nano Lett.* **17**(5), 2757 (2017).
- <sup>47</sup>C. Xie, Z. Lin, L. Hanson, Y. Cui, and B. Cui, *Nat. Nanotechnol.* **7**, 185 (2012).
- <sup>48</sup>A. Aalipour, A. M. Xu, S. Leal-Ortiz, C. C. Garner, and N. A. Melosh, *Langmuir* **30**, 12362 (2014).
- <sup>49</sup>M. E. J. Obien, K. Deligkaris, T. Bullmann, D. J. Bakkum, and U. Frey, *Front. Neurosci.* **9**, 423 (2015).
- <sup>50</sup>L. Berdondini, M. Chiappalone, P. D. Van Der Wal, K. Imfeld, N. F. De Rooij, M. Koudelka-Hep, M. Tedesco, S. Martinoia, J. Van Pelt, G. L. Masson, and A. Garenne, *Sens. Actuat. B Chem.* **114**, 530 (2006).
- <sup>51</sup>V. Viswam, M. E. J. Obien, F. Franke, U. Frey, and A. Hierlemann, *Front. Neurosci.* **13**, 385 (2019).
- <sup>52</sup>X. Xie, A. M. Xu, M. R. Angle, N. Tayebi, P. Verma, and N. A. Melosh, *Nano Lett.* **13**, 6002 (2013).
- <sup>53</sup>A. Hai and M. E. Spira, *Lab Chip* **12**, 2865 (2012).
- <sup>54</sup>J. Abbott, T. Ye, L. Qin, M. Jorgolli, R. S. Gertner, D. Ham, and H. Park, *Nat. Nanotechnol.* **12**, 460 (2017).
- <sup>55</sup>M. Dipalo, H. Amin, L. Lovato, F. Moia, V. Caprettini, G. C. Messina, F. Tantussi, L. Berdondini, and F. De Angelis, *Nano Lett.* **17**, 3932 (2017).
- <sup>56</sup>D. A. Robinson, *Proc. IEEE* **56**, 1065 (1968).
- <sup>57</sup>G. E. Loeb, R. A. Peck, and J. Martyniuk, *J. Neurosci. Methods* **63**, 175 (1995).
- <sup>58</sup>E. W. Keefer, B. R. Botterman, M. I. Romero, A. F. Rossi, and G. W. Gross, *Nat. Nanotechnol.* **3**, 434 (2008).
- <sup>59</sup>W. Franks, I. Schenker, P. Schmutz, and A. Hierlemann, *IEEE Trans. Biomed. Eng.* **52**, 1295 (2005).
- <sup>60</sup>S. F. Cogan, *Annu. Rev. Biomed. Eng.* **10**, 275 (2008).
- <sup>61</sup>J. T. Robinson, M. Jorgolli, A. K. Shalek, M. H. Yoon, R. S. Gertner, and H. Park, *Nat. Nanotechnol.* **7**, 180 (2012).
- <sup>62</sup>Y. Bi and J. Ye, *Chem. Commun.* **43**, 6551 (2009).
- <sup>63</sup>M. Ganji, A. T. Elthakeb, A. Tanaka, V. Gilja, E. Halgren, and S. A. Dayeh, *Adv. Funct. Mater.* **27**, 1703018 (2017).
- <sup>64</sup>M. Ganji, E. Kaestner, J. Hermiz, N. Rogers, A. Tanaka, D. Cleary, S. H. Lee, J. Snider, M. Halgren, and G. R. Cosgrove, *Adv. Funct. Mater.* **28**, 1700232 (2018).
- <sup>65</sup>J. Rivnay, S. Inal, B. A. Collins, M. Sessolo, E. Stavrinidou, X. Strakosas, C. Tassone, D. M. Delongchamp, and G. G. Malliaras, *Nat. Commun.* **7**, 11287 (2016).
- <sup>66</sup>J. Rivnay, H. Wang, L. Fenno, K. Deisseroth, and G. G. Malliaras, *Sci. Adv.* **3**, e1601649 (2017).
- <sup>67</sup>S. Negi, R. Bhandari, L. Rieth, and F. Solzbacher, *Biomed. Mater.* **5**, 15007 (2010).
- <sup>68</sup>M. Ganji, A. Tanaka, V. Gilja, E. Halgren, and S. A. Dayeh, *Adv. Funct. Mater.* **27**, 1703019 (2017).
- <sup>69</sup>X. Duan, R. Gao, P. Xie, T. Cohen-Karni, Q. Qing, H. S. Choe, B. Tian, X. Jiang, and C. M. Lieber, *Nat. Nanotechnol.* **7**, 174 (2012).
- <sup>70</sup>D. B. Suyatin, L. Wallman, J. Thelin, C. N. Prinz, H. Jörntell, L. Samuelson, L. Montelius, and J. Schouenborg, *PLoS One* **8**, e56673 (2013).
- <sup>71</sup>G. Buzsáki, C. A. Anastassiou, and C. Koch, *Nat. Rev. Neurosci.* **13**, 407 (2012).
- <sup>72</sup>W. Zhou, X. Dai, and C. M. Lieber, *Rep. Prog. Phys.* **80**, 016701 (2017).
- <sup>73</sup>C. Chiappini, *ACS Sens.* **2**, 1086 (2017).
- <sup>74</sup>R. Liu, J. Lee, Y. Tchoue, D. Pre, A. M. Bourhis, A. D’Antonio-Chronowska, G. Robin, S. H. Lee, Y. G. Ro, R. Vatsyayan, K. J. Tonsfeldt, L. A. Hossain, M. L. Phipps, J. Yoo, J. Nogan, J. S. Martinez, K. A. Frazer, A. G. Bang, and S. A. Dayeh, *Adv. Funct. Mater.* **21**, 2108378 (2021).
- <sup>75</sup>M. E. Spira, N. Shmoel, S. H. M. Huang, and H. Erez, *Front. Neurosci.* **12**, 212 (2018).
- <sup>76</sup>N. Shmoel, N. Rabieh, S. M. Ojovan, H. Erez, E. Maydan, and M. E. Spira, *Sci. Rep.* **6**(1), 27110 (2016).
- <sup>77</sup>Z. C. Lin, A. F. McGuire, P. W. Burrige, E. Matsa, H. Y. Lou, J. C. Wu, and B. Cui, *Microsyst. Nanoeng.* **3**, 16080 (2017).
- <sup>78</sup>H. B. Hayes, A. M. Nicolini, C. A. Arrowood, S. A. Chvatal, D. W. Wolfson, H. C. Cho, D. D. Sullivan, J. Chal, B. Fermini, M. Clements, J. D. Ross, and D. C. Millard, *Sci. Rep.* **9**, 11893 (2019).
- <sup>79</sup>M. Dipalo, S. K. Rastogi, L. Martino, R. Garg, J. Bliley, G. Iachetta, G. Melle, R. Shrestha, S. Shen, F. Santoro, A. W. Feinberg, A. Barbaglia, T. Cohen-Karni, and F. De Angelis, *Sci. Adv.* **7**, eabd5175 (2021).
- <sup>80</sup>G. C. Messina, M. Dipalo, R. La Rocca, P. Zilio, V. Caprettini, R. Proietti Zaccaria, A. Toma, F. Tantussi, L. Berdondini, and F. De Angelis, *Adv. Mater.* **27**, 7145 (2015).
- <sup>81</sup>F. De Angelis, M. Malerba, M. Patrini, E. Miele, G. Das, A. Toma, R. P. Zaccaria, and E. Di Fabrizio, *Nano Lett.* **13**, 3553 (2013).
- <sup>82</sup>B. X. E. Desbiolles, E. De Coulon, A. Bertsch, S. Rohr, and P. Renaud, *Nano Lett.* **19**, 6173 (2019).
- <sup>83</sup>B. X. E. Desbiolles, E. de Coulon, N. Maïno, A. Bertsch, S. Rohr, and P. Renaud, *Microsyst. Nanoeng.* **6**, 67 (2020).
- <sup>84</sup>Y. Liu, A. F. McGuire, H. Y. Lou, T. L. Li, J. B. H. Tok, B. Cui, and Z. Bao, *Proc. Natl. Acad. Sci. U. S. A.* **115**, 11718 (2018).
- <sup>85</sup>K. Peng, Y. Xu, Y. Wu, Y. Yan, S. T. Lee, and J. Zhu, *Small* **1**, 1062 (2005).
- <sup>86</sup>E. C. Garnett and P. Yang, *J. Am. Chem. Soc.* **130**, 9224 (2008).
- <sup>87</sup>K. Balasundaram, J. S. Sadhu, J. C. Shin, B. Azeredo, D. Chanda, M. Malik, K. Hsu, J. A. Rogers, P. Ferreira, S. Sinha, and X. Li, *Nanotechnology* **23**, 305304 (2012).
- <sup>88</sup>P. K. Mohseni, S. H. Kim, X. Zhao, K. Balasundaram, J. D. Kim, L. Pan, J. A. Rogers, J. J. Coleman, and X. Li, *J. Appl. Phys.* **114**, 64909 (2013).
- <sup>89</sup>W. Tang, B. M. Nguyen, R. Chen, and S. A. Dayeh, *Semicond. Sci. Technol.* **29**, 054004 (2014).
- <sup>90</sup>X. Xie, A. Aalipour, S. V. Gupta, and N. A. Melosh, *ACS Nano* **9**, 11667 (2015).
- <sup>91</sup>A. Solanki and H. Um, *Top-Down Etching of Si Nanowires*, 1st ed. (Elsevier Inc., 2018).
- <sup>92</sup>G. W. Rubloff, K. Hofmann, M. Liehr, and D. R. Young, *Phys. Rev. Lett.* **58**, 2379 (1987).
- <sup>93</sup>S. Majee, D. Barshilia, S. Kumar, P. Mishra, and J. Akhtar, *AIP Conf. Proc.* **1989**, 020023 (2018).

- <sup>94</sup>A. Zhang and C. M. Lieber, *Chem. Rev.* **116**, 215 (2016).
- <sup>95</sup>J. Yoo, H. Kwak, J. Kwon, G. E. Ha, E. H. Lee, S. Song, J. Na, H. J. Lee, J. Lee, A. Hwangbo, E. Cha, Y. Chae, E. Cheong, and H. J. Choi, *Sci. Rep.* **10**, 4279 (2020).
- <sup>96</sup>B. Tian, T. Cohen-Karni, Q. Qing, X. Duan, P. Xie, and C. M. Lieber, *Science* **329**, 830 (2010).
- <sup>97</sup>G. C. Yi, C. Wang, and W. Il Park, *Semicond. Sci. Technol.* **20**, S22 (2005).
- <sup>98</sup>H. Baek, H. Kwak, M. S. Song, G. E. Ha, J. Park, Y. Tchoe, J. K. Hyun, H. Y. Park, E. Cheong, and G.-C. Yi, *APL Mater.* **5**, 046106 (2017).
- <sup>99</sup>K. Tomioka, T. Tanaka, S. Hara, K. Hiruma, and T. Fukui, *IEEE J. Sel. Top. Quantum Electron.* **17**, 1112 (2011).
- <sup>100</sup>Y. J. Hong, H. S. Jung, J. Yoo, Y. Kim, C. Lee, M. Kim, and G. Yi, *Adv. Mater.* **21**, 222 (2009).
- <sup>101</sup>N. Hu, D. Xu, J. Fang, H. Li, J. Mo, M. Zhou, B. Li, H. jiu Chen, T. Zhang, J. Feng, T. Hang, W. Xia, X. Chen, X. Liu, G. He, and X. Xie, *Biosens. Bioelectron.* **169**, 112588 (2020).
- <sup>102</sup>W. W. Lee, J. Yi, S. B. Kim, Y. H. Kim, H. G. Park, and W. Il Park, *Cryst. Growth Des.* **11**, 4927 (2011).
- <sup>103</sup>H. Liu, O. A. Bolonduro, N. Hu, J. Ju, A. A. Rao, B. M. Duffy, Z. Huang, L. D. Black, and B. P. Timko, *Nano Lett.* **20**, 2585 (2020).
- <sup>104</sup>Z. C. Lin, C. Xie, Y. Osakada, Y. Cui, and B. Cui, *Nat. Commun.* **5**, 3206 (2014).
- <sup>105</sup>C. Xie, L. Hanson, W. Xie, Z. Lin, B. Cui, and Y. Cui, *Nano Lett.* **10**, 4020 (2010).
- <sup>106</sup>J. J. Vandersarl, A. M. Xu, and N. A. Melosh, *Nano Lett.* **12**, 3881 (2012).
- <sup>107</sup>P. Apel, *Radiat. Meas.* **34**, 559 (2001).
- <sup>108</sup>E. Peer, A. Artzy-Schnirman, L. Gepstein, and U. Sivan, *ACS Nano* **6**, 4940 (2012).
- <sup>109</sup>T. M. Fu, X. Duan, Z. Jiang, X. Dai, P. Xie, Z. Cheng, and C. M. Lieber, *Proc. Natl. Acad. Sci. U. S. A.* **111**, 1259 (2014).
- <sup>110</sup>Y. Su, C. Liu, S. Brittman, J. Tang, A. Fu, N. Kornienko, Q. Kong, and P. Yang, *Nat. Nanotechnol.* **11**, 609 (2016).
- <sup>111</sup>X. W. Zhang, Q. F. Qiu, H. Jiang, F. L. Zhang, Y. L. Liu, C. Amatore, and W. H. Huang, *Angew. Chem.—Int. Ed.* **56**, 12997 (2017).
- <sup>112</sup>R. Singhal, Z. Orynbayeva, R. V. K. Sundaram, J. J. Niu, S. Bhattacharyya, E. A. Vitol, M. G. Schrlau, E. S. Papazoglou, G. Friedman, and Y. Gogotsi, *Nat. Nanotechnol.* **6**, 57 (2011).
- <sup>113</sup>G. He, N. Hu, A. M. Xu, X. Li, Y. Zhao, and X. Xie, *Adv. Funct. Mater.* **30**, 2070200 (2020).
- <sup>114</sup>M. Dipalo, V. Caprettini, G. Bruno, F. Caliendo, L. D. Garma, G. Melle, M. Dukhinova, V. Siciliano, F. Santoro, and F. De Angelis, *Adv. Biosyst.* **3**, e1900148 (2019).
- <sup>115</sup>C. Y. Lee, C. L. Chang, Y. N. Wang, and L. M. Fu, *Int. J. Mol. Sci.* **12**, 3263 (2011).
- <sup>116</sup>M. L. Khraiche and R. E. Hassan, *J. Sci. Adv. Mater. Devices* **5**, 279 (2020).
- <sup>117</sup>H. Y. Lou, W. Zhao, Y. Zeng, and B. Cui, *Acc. Chem. Res.* **51**, 1046 (2018).
- <sup>118</sup>S. Bonde, J. Bolinsson, T. Berthing, and K. L. Martinez, *Adv. Funct. Mater.* **25**, 3246 (2015).
- <sup>119</sup>J. Zhou, X. Zhang, J. Sun, Z. Dang, J. Li, X. Li, and T. Chen, *Phys. Chem. Chem. Phys.* **20**, 22946 (2018).
- <sup>120</sup>R. Capozza, V. Caprettini, C. A. Gonano, A. Bosca, F. Moia, F. Santoro, and F. De Angelis, *ACS Appl. Mater. Interfaces* **10**, 29107 (2018).
- <sup>121</sup>A. M. Ross, Z. Jiang, M. Bastmeyer, and J. Lahann, *Small* **8**, 336 (2012).
- <sup>122</sup>V. Gautam, S. Naureen, N. Shahid, Q. Gao, Y. Wang, D. Nisbet, C. Jagadish, and V. R. Daria, *Nano Lett.* **17**, 3369 (2017).
- <sup>123</sup>M. Ghibaud, L. Trichet, J. L. Digabel, A. Richert, P. Hersen, and B. Ladoux, *Biophys. J.* **97**, 357 (2009).
- <sup>124</sup>M. S. Lord, M. Foss, and F. Besenbacher, *Nano Today* **5**, 66 (2010).
- <sup>125</sup>H. Shadpour and N. L. Allbritton, *ACS Appl. Mater. Interfaces* **2**, 1086 (2010).
- <sup>126</sup>T. Y. Chang, V. G. Yadav, S. De Leo, A. Mohedas, B. Rajalingam, C.-L. Chen, S. Selvarasah, M. R. Dokmeci, and A. Khademhosseini, *Langmuir* **23**, 11718 (2007).
- <sup>127</sup>A. Cerea, V. Caprettini, G. Bruno, L. Lovato, G. Melle, F. Tantussi, R. Capozza, F. Moia, M. Dipalo, and F. De Angelis, *Lab Chip* **18**, 3492 (2018).
- <sup>128</sup>J. Kwon, S. Ko, J. Lee, J. Na, J. Sung, H. J. Lee, S. Lee, S. Chung, and H. J. Choi, *Nanoscale* **12**, 4709 (2020).